Title
Carbon-based Materials for Energy Storage

Author
Rice, Lynn Margaret

Publication Date
2012

Peer reviewed|Thesis/dissertation

UNIVERSITY OF CALIFORNIA

Los Angeles

Carbon-based Materials for Energy Storage

A dissertation submitted in partial satisfaction of the

requirements for the degree Master of Science

in Chemical Engineering

by

Lynn Margaret Rice

2012

ABSTRACT OF THE THESIS

Carbon-based Materials for Energy storage

by

Lynn Margaret Rice
Master of Science in Chemical Engineering
University of California, Los Angeles, 2012
Professor Yunfeng Lu, Chair

Fossil fuels can be burned to provide on-demand energy at any time, but cleaner renewable energy sources such as the sun and wind are intermittent. Energy storage systems, then, that are efficient and also economical and environmentally benign are key to a future fueled by renewable energy. Carbon-based materials are prototypical systems in all these aspects.

Herein, three promising, novel carbon-based materials are presented. These include microporous carbon for supercapacitors produced by the condensation and carbonization of siloxane elastomers, porous graphitic carbon for supercapacitors produced by an aerosol route, and interpenetrating, binder-free carbon nanotube/vanadium nanowire composites for lithium ion battery electrodes produced by chemical crosslinking and aerogel fabrication. These materials syntheses are facile and can be easily scaled up, and their electrochemical performance, especially their energy densities and cycleability, are notable

The thesis of Lynn Margaret Rice is approved.

_____

Selim Senkan

_____

Harold Monbouquette

_____

Yunfeng Lu, Chair

University of California, Los Angeles

2012

DEDICATION

To Dr. Lu, a longtime mentor, for sparking my interest in nanotechnology and in China and providing me outlets to explore and grow both of those interests. With gratitude for the support and opportunities you've provided me, the friends you've introduced me to, and for inspiration along the way: Thanks for everything.

TABLE OF CONTENTS

INTRODUCTION

A. Background and Significance of Research

We enter the 21st with the supply of nonrenewable resources on which we depend fading. Energy from renewable sources such as hydroelectric dams, wind turbines and solar panels is staked to supplement and even replace that of fossil fuels. The energy from these clean technologies, though, is low density and highly intermittent[1].

Our success in transitioning to a renewable energy-fueled future is therefore contingent on the development of appropriate power electronics[2] and on energy storage systems that enable us to use the sum of energy we require whether or not the sun is shining or the wind blowing. In order to ensure delivery of energy over a suitable time scale and at an appropriate power level, batteries and capacitors must be improved:

The lithium ion battery is the current superstar in the field of energy storage. Energy-dense lithium ion batteries have evolved immensely since their commercialization in the 1980s. Currently, they are widely used in electronic devices such as cellular phones, notebook computers and AV equipment, and inroads are even being made in their use in hybrid electric and electric vehicles. Still, several challenges impede their efficacy in these devices including safety problems and poor power density due to slow kinetics.

A complement to energy dense, low power lithium ion batteries is high power capacitors. Capacitors are used in tandem with batteries to level and amplify their load.

Capacitor technology has undergone enormous strides since the inception of supercapacitors[3] whose specific energy and specific capacitance are hundreds and thousands of times that of conventional capacitors, respectively[4]. Supercapacitors have been successfully applied in auxiliary energy systems that account for acceleration and regenerative braking in hybrid electric vehicles[5] and are particularly desirable in these applications due to their compact nature.

The burgeoning of nanotechnology has been a boon to the development of batteries and capacitors. Due to their high surface area (up to over 3,000 m^2/g for microporous carbon, for example) and unique interfacial characteristics, nanomaterials exhibit often-unpredictable electronic properties not present in the bulk phase. Since energy in electrochemical storage systems is stored on surfaces, high surface area materials typically exhibit enhanced electrochemical performance.

Moreover, advanced characterization techniques, especially electron microscopy, provide scientists and engineers a means to accurately observe pore structure at the nanoscale. We can, but haven't yet substantially, used these tools to rigorously correlate pore size and architecture to a multitude of electrochemical performance parameters. Doing so will turn our quest for advanced electrochemical materials from the current vein that relies heavily on empiricism to a more predictive approach.

Therefore, although we enter the 21st century in the early stages of a global energy crisis, we enter, too, with promise for an approach to future energy that is cleaner, more

sustainable and more smartly designed than present systems. We enter with the data from electrochemical studies that have spanned centuries at our fingertips and with access to unprecedented nanoscale characterization techniques that enable us to forge a long-overdue energy revolution.

B. Supercapacitors Materials Background

Supercapacitors, also referred to as electrochemical capacitors or ultracapacitors, sacrifice the extremely high power density and low energy density of traditional dielectric capacitor materials in favor of only relatively high power density and improved energy density. They occupy a position on the Ragone plot intermediate batteries and dielectric capacitors. Other key characteristics of supercapacitors include ultrafast charging and discharging and extremely high cycleability. State of the art supercapacitors boast ultrafast charge and discharge times on the order of one second, energy densities of around 5 Wh/kg, power densities of 5-10 Wh/kg and can withstand more than 500,000 cycles[6].

Given such electrochemical performance, supercapacitors have applications in a wide range of electrical devices with high energy and power demands over time scales of 10^{-2} to 10^{2} seconds in DC systems[4]. Examples include auxiliary energy systems for hybrid electric vehicles[5], uninterruptable power supply systems (UPS)[7] and backup power booster charging.

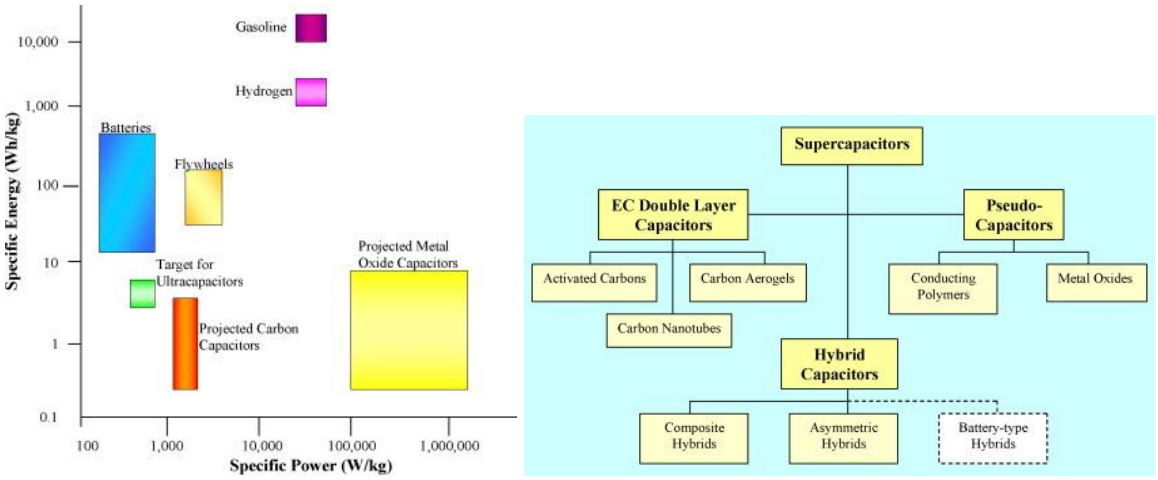

Figure 1: Ragone plot comparing various energy storage systems, left, and supercapacitor taxonomy, right[34]

Among supercapacitors are electrochemical double layer capacitors (EDLCs), which operate via a non-Faradaic double layer mechanism where charge is stored statically at the interface between electrode and electrolyte. Such electrode materials don't undergo the electrochemical reactions present in batteries. Other types of supercapacitors include pseudo capacitors[8] and, more recently, hybrid capacitors which have asymmetric or composite type electrodes that incorporate the metal oxides or conducting polymers used in psuedocapacitors with the carbons used in EDLCs[9]. Figure one illustrates the taxonomy of supercapacitor systems and the main constituents of each.

At present, EDLCs are both the most economical to produce and the most prevalent type of supercapacitor. EDLCs were first conceived in 1957 with a patent by Becker[3]. From thereon, mesoporous carbons were primarily used in their construction,

and research efforts over the years have been centered on developing optimal mesopore morphologies and ordering to facilitate ultrafast charge transfer at the electode/electrolyte interface[10, 16]. Recently, it has been established that microporous carbon EDLCs offer higher capacitance than EDLCs based on mesoporous carbon alone due to their larger surface areas available for charge storage and also due to a poorly understood mechanism that could involve ions' removal from a solvation sheath[11].

Given the superior performance of microporous carbons over mesoporous carbons in EDLCs, synthetic methods that are cost effective and efficient and that impart their products with narrow, mainly microporous pore size distributions and good pore connectivity are a subject of present interest. While energy density is inevitably gained at the sacrifice of power density, a major thrust in current energy research and development is improving the energy density of EDLCs without significant sacrifice of power density. Key factors in improving energy density in capacitor materials while retaining high power density are increasing surface area around which the double layer can develop and accelerating ion transport during charging and discharging. Concerning the former, the greater the fraction of microporosity is within carbon material, the higher its surface area and hence energy density. This concept, though, is practically limited by ion transfer. Small pores that aren't adequately connected will trap ions, reducing power density. Therein lies the need to make microporous materials with long term ordering and regularly connected pores.

C. State of the Art

Techniques for fabricating microporous carbon materials (pores less than 2 nm) are considerably less numerous and developed than those for fabricating mesoporous (pores 2-50 nm) and hierarchically porous (incorporating micro, meso and/or macropores) materials. A plethora of forms of carbon remain under exploration, including aerogels, xerogels, fibers, conducting polymers and carbon nanotubes, to name a few[12]. The most common synthetic techniques towards microporous carbons include physical and chemical activation of organic and inorganic materials, and templated synthesis. Their advantages and drawbacks are discussed herein

a. Activated Carbons

Activated Carbons are obtained from pyrolysis (over 800˚ C) in the absence of air followed by chemical and/or physical activation of carbon rich starting materials. In chemical activation, activation agents such as $ZnCl_2$, H_3PO_4, KOH, K_2S KCNS are applied to the starting materials and removed after carbonization via washing. In physical activation, materials are subjected to steam, CO2, air or some combination therein and portions of the starting materials are partially gasified in these process streams[13]. A wide range of precursors have been successfully converted into activated carbons, from coal and pitch derivatives[14] to sucrose, coffee grounds, macadamia nut shells, and polymers such as polyvinylidene chloride and furan based polymers[15]. Activated Carbons, moreover, can be employed in a variety of forms including activated carbon fibers[29], cloths, powders, and composites thereof[30].

Depending on the starting material, activated carbons can take on a range of pore size distributions, which intimately affects their capacitance and series cell resistance[17] Activated Carbons generally have high BET surface areas in the range of 1000 to 2000 m2/g and capacitances between 100 and 200 F/g in aqueous electrolytes[18]. While capacitance is generally proportional to surface area, but this relationship finds repeated exceptions which are attributable to the effects of pore size and connectivity on capacitance [19, 20].

Their reasonably straightforward processing and high surface areas makes them the leading material for supercapacitors today. A disadvantage of activated carbons, though is that the final properties are based on the structure of the often naturally occuring starting materials, rendering tuning the properties for a specific purpose challenging. Activated carbons also often contain a large number of surface functional groups and defects, lowering their conductivity [31].

b. Templated Carbons

The templated synthesis of carbon generally includes four steps: preparation of a template, impregnation or infiltration of carbon precursors into that template, cross-linking and carbonization of precursor materials and, finally, removal, i.e. via dissolution, of the template.

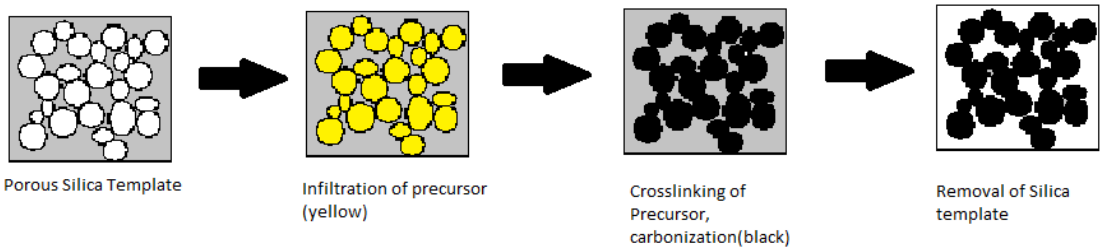

Figure 2: Templated Carbon Synthetis Schematic

A wide range of templates of both hard and, more recently, soft template can be used to make templated, porous carbon. The use of hard templates, especially zeolites and molecular sieves, are current leading methods for micropourous carbon production. The first report of templated carbon came from Knox in 1983[21] while the first self-supported, ordered template carbon was synthesized by Ryoo[22] using molecular sieve MCM-48 as the hard template. Both synthetic and naturally occurring zeolites have been explored as templates for producing microporous carbons[42]. While zeolite-templated carbon exhibits extremely high surface area, significant microporosity and long range ordering(for example, zeolite Y-templated carbon has a surface area of 3600 m^2/g), until recently, researchers had been unable to replicate the pore structure of the original zeolite material onto the template material. This changed in 2001 when Kyotani developed a two-step process consisting of impregnation of carbon precursors into zeolite templates followed by chemical vapor deposition[23].

Initial application of molecular sieve-templated carbons and zeolite-templated carbons to supercapacitors has been relatively successful. Béguin and coworkers have reported gravimetric capacitance of 110 F/g in aqueous electrolyte for MCM-48 templated carbons[24]. The approach of further modifying templated carbons has also been successful. Recently, Béguin and group have doped zeolite templated carbon with nitrogen[25]. The resulting enhanced microporous carbon displayed an impressive 340 F/g capacitance in aqueous electrolyte.

Anodized Alumina templates (AAO) have also been used to create carbon nanotubes[26] which have found great promise in their application to supercapacitors[27,28].

The main disadvantages of employing templating as a means to synthesize porous carbon are the time and cost, especially in processes where the templates must first be created.

A panoply of techniques has been used to fabricate porous carbon for battery and capacitor electrodes, yet activated carbons and graphitized carbons lacking advanced microstructures and adhered together and to current collectors by non-conductive polymeric binders remain the industrial norm[12].

Introduction References:

1. Kessides, Ioannis N. and Wade, David C., (January 1, 2011). World Bank Policy Research Working Paper Series, no. 5539, 2011.

2. Chakraborty, S., Kramer, B. and Kroposki, B. Renewable and Sustainable Energy Reviews, Volume 13, Issue 9, Pages 2323-2335 (2009)

3. Becker, H.E., US Patent 2 800 616 (to General Electric) (1957)
4. Kötz, R. and Carlen, M. Electrochimica Acta 45, 2483-2498 (2000)
5. Ortuzar, M; Moreno J. and Dixon, J., IEE Transactions on Industrial Electronics, v. 54, #4, 2147-2156 (2007)
6. Miller, J. R. and Burke, A. The Electrochemical Society Interface Spring 2008
7. Galkin, I.; Stepanov, A. and Langis, J. Baltic Electronics Conference, 2006 International, pgs 1-4, 2-4 Oct 2006
8. Conway, B.E.; Birss, V. and Wojtowicz, J. Journal of Power Sources 66, 1-14 (1997)
9. Simon, P. and Gogotsi, Y. Nature Materials 7, 845-854 (2008)
10. Jurewicz, K.; Vix_Guterl, C. ; Frackowiak, E.' Saadallah, S.; Reda, M.; Parmentier, J.; Patarin, J. and Béguin, F. Journal of Physics and Chemistry of Solids 65, 287-293 (2007)
11. Chmiola, J.; Largeot, C.; Taberna, P.; Simon, P. and Gogotsi, Y. Angew. Chem. Int. Ed. 47, 3392-3395 (2008)
12. Frackowiak, E. and Béguin, F. Carbon 39, 937-950 (2001)
13. Wigmans, T. Carbon 27, 13-22 1989

14. Kierzek, K.; Frackowiak, E.; Lota, G.; Gryglewicz, G.; Machnikowski, J. Electrochimica Acta 49, 515-523 (2004)
15. Evans, M.J.B.; Halliop, E. and MacDonald, J.A.F.; Carbon 37, 2, 269-274 (1999)
16. Vix-Guterl, C.; Frackowiak, E.; Jurewicz, K.; Friebe, M.; Parmentier, J.; and Beguin, F. Carbon 43, 1293-1302 (2005)
17. Gamby, J.; Taberna, P.; Simon, P.; Fauvarque, J. and Chesneau, M. Journal of Power Sources 101, 109-116 (2001)
18. Frackowiak, E. Phys. Chem. Chem. Phys., 2007, 9, 1774-1785 (2007)
19. Qu, D. and Shi, H. J. Power Sourc 74(1), 99-107 (1998)
20. Shi, H. Carbon 97, 826-827 (1997)
21. Knox, J.H.; Unger, K.K. and Mueller, H. J. Liq. Chromatogr. 6,1 (1983)
22. Ryoo, R.; Joo, S; and Jun, S. J.P. Chem B, 103, 37, 7743-7746 (1999)
23. Ma, Z.X.; Kyotani, T.; Liu, Z.; Terasaki, O. and Tomita, A. Chem Mater 13, 4413 (2001)
24. Vix-Guterl, C.; Saadallah, S.; Jurewic, K. and Beguin, F. et. al Materials Science and Engineering B 108, 1-2, 148-155 (2004)
25. Ania, C.O.; Khomenko, V., Raymundo-Piñero, E.; Parva, J. and Béguin, F. Advanced Functional Materials 17, 11, 1828-1836 (2007)
26. Suh, J.S. and Lee, J.S. Appl Phys Letters 75, 154, 2047-2050
27. Frackowiak, E.; Metenier, K.; Bertagna, V. and Beguin, F. Applied Physics Letters 77, 15, 2421-2423 (2000)

28. Lee, S.W.; Kim, B.; Chen, S. Shao-Horn, Y.; and Hammond, P. J. Am. Chem. Soc. 131, 671-679 (2009)

29. Suzuki, M. Carbon, Volume 32, Issue 4, Pages 577-586 (1994)

30. Noked, M., Soffer, A.and Aurbach, D. Journal of Solid State Electrochemistry v15, p 1563-1578 (2011)

31. Wang, RQ, Deng, MG. Advanced Materials Research v347-353, p. 3456-3458 (2012)

32. Burke, A. Electrochimica Acta 53, 1083-1091 (2007)

33. Fawcett, J. and Camerman, M. Can. J. Chem 55, 3631-3635 (1977)

34. Hadjipachalis, I.; Poullikkas, A. and Efthimiou, V. Renewable and Sustainable Energy Reviews 13, 1513-1522 (2009)

35. Hyde, J.F. and DeLong, R.C. J Am. Chem Soc 63 (5), 1194-1196 (1941)

36. Kresge, C.T.; Leonowicz, M.E.; Roth, W.J.; Vartuli, J.C. and Beck, J.S. Nature 359, 710-712 (1992)

37. Kristenmacher, T.J.; Rossi, M.; Frevel, L.K. J Appl Cryst 11, 670-671 (1978)

38. Kyotani, T.; Ma, Z. and Tomita, A. Carbon 41, 7, 1451-1459 (2003)

39. Ma Z.X.; Kyotani T. and Tomita A. Chem Commun 2365–66 (2000)

40. Morimoto, T.; Hiratsuka, K.; Sanada, Y. and Aruga, H. US Patent 4,725,927 (1988), to Asahi Glass Co. and Elna Co. Ltd.

41. Winter, M. and Brodd, R. Chem. Rev. 2004, 104, 4245-4269 (2004)

42. Ania, C. O., Khomenko, V., Raymundo-Piñero, E., Parra, J. B. and Béguin, F. Adv. Funct. Mater. v17 pgs 1828-1836 (2007)

CHAPTER 1

Microporous Carbon for Supercapacitors Prepared by the Facile Condensation of Elastomers

Chapter 1 Statement of Contribution: The, to date, unpublished work in this communication was conducted as an individual project with the aid of training and valuable discussions from Zheng Chen and Xilai Jia,

Abstract Polydiphenylsiloxane (PdPhs) elastomers have been carbonized, giving rise to dense, conductive carbon/silicon composites. Etching silicon from these matrices leaves an abundance of regularly distributed micropores, resulting in highly porous carbon for supercapacitors. Such carbon has a tunable microstructure with capacitance of up to 223 F/g in aqueous electrolyte. Moreover, this novel route was shown to be easily tunable by varying the condensation parameters, including using tetraethylorthosilicate (TEOS) as a template and by catalytically graphitizing the carbon during pyrolysis, and hence lays the groundwork for future carbon materials based on this synthetic approach.

Communication Electical double layer capacitors (EDLCs or supercapacitors) have a wide range of applications from auxiliary energy systems for hybrid electric vehicles [1-1] to uninterruptable power supply systems (UPS) [1-2] to back up power booster charging[1-4]. The longest lasting, most widespread supercapacitors currently in use are constructed from porous carbon:

Porous carbon for supercapacitors should have high surface area in order to accommodate a large number of ions, since theoretical capacitance increases according to surface area[1-3]. High surface area tends to result in high energy density[1-5].

Since only accesible surface area can contribute to capacitance, though, open and regular pore structures that faciltate rapid ion transport are likewise critcal to EDLC performance. Open, narrowly distributed pores in electrodes that match electrolyte ions' dimensions result in the high power density and rate capability for which supercapacitors are renowned [1-6, 1-7].

Ubiquitous activated carbons have extremely high surface area (>2000 m^2/g) and the details of their activation and processing have been tuned extensively[1-8, 1-9, 1-10,1-11] Due to lack of control on the nanoscale during activation, though, their pores are generally tortuous and bottlenecked. Such morphology can result in cation trapping at the negative electrode[1-12]. Also, their pore size distributions are large, varying from 0.3-4 nanometers, where smaller pores are inaccessible to electrolyte ions and larger pores aren't optimally filled.

Carbide derived carbons, which are generated through the selective etching of non carbon species in metal carbides such as silicon carbide and boron carbide, have been synthesized to overcome the limitations in controlling pore size encountered in activated carbons. Tuning their pore size distributions by controlling chlorination time and temperature has been demonstrated[1-13, 1-7]. Their synthesis is costly and low yield, though.

Herein, we report a novel route towards microporous carbon with an open pore structure, a narrow pore size distribution and high capacitance. Its facile synthesis proceeds via solution condensation: polysiloxane elastomers are formed by condensing carbon-dense diphenylsilane diol in solution in the presence of acid catalyst. This elastomer's condensation is depicted in figure n. Condensation commences at room temperature. Polymerization continues at 120˚ C where chains develop and the elastomer takes on a characteristic stickiness. Heating the elastomer between 180˚C and 210˚C in a nitrogen atmosphere, 20% weight loss occurs (as confirmed by thermal gravimetric analysis) that corresponds to liberation of water with additional condensation. As the temperature is ramped between 210˚C and 600˚C under nitrogen, an additional 30% weight loss occurs that corresponds to the densification of the carbon chains. After sintering up to 900˚C and silicon removal through an acid etch, a high capacitance microporous carbon remains.

A variety of synthetic schemes were tested to arrive at the chosen weak acid condensation. They include condensation in the presence of a stronger acid catalyst (0.5 M HCL compared to the weaker 0.02 M HCL catalyst) as well as a stronger (0.5M KOH) and weaker (0.02M KOH) base catalyst. Condensation and carbonization in the presence of nickel salt (5 w/w% nickel nitrate hexahydrate) was used to promote graphitization, tetrarthyl orthosilicate (TEOS), 10 w/w% was added to form channels via templating of silicate clusters, and, in another experiment, the surfactant F127 was added along with TEOS 1:1 w:w (referred to in the table 1 as 100 wt% TEOS) to form a carbon material

based on triconstituent coassembly. The resulting materials' surface area and capacitances are listed in table 1 below:

Treatment	Surface Area m2/g	Capacitance in F/g at 2 mV/s	Capacitance in F/g at 20 mV/s
Strong Base	1466	170	128
Weak Base	109	X	X
Strong Acid	1692	156	105
Weak Acid	2275	175	132
Nickel Salt	766	174	109
10 wt% TEOS	1328	130	95
100 wt% TEOS +F127	3125	223	182

Table 1-1: Surface Area and capacitance of carbons produced from carbonized PdPhs that was condensed using a variety of catalysts

Strong acid and strong base catalyses yield materials with relatively high surface areas and similar pore size distributions to the weak acid catalyzed materials:

The strong base catalyzed materials, despite their comparatively lower surface areas, display similar capacitance to the weak acid catalyzed carbon. Especially since KOH

could also be exploited for its activation effect, such materials are also good candidates for the active mass in supercapacitor electrodes.

The strong acid catalyzed materials display somewhat lower capacitance that results from ultrafast PdPhs condensation. Rapid condensation doesn't allow time for the condensed chains to stack well and hence some pores are blocked. Those inaccessible pores lower the overall capacitance.

Addition of nickel salts results in a well-graphitized structure that was confirmed through X-ray diffraction. Nickel-catalyzed PdPhs carbon displayed characteristic graphitic peaks at $2\theta = 26.6$, 42.5 and 54.5 degrees. Densification resulted in significant loss of surface area, though, and a widening of the pore channels, with an average pore diameter of 5.5 nm. The graphitized porous carbon obtained did not have good rate capability as a result of pore walls that collapsed during graphitization.

TEOS incorporation into the precursor, as predicted, lowered the surface area and shifted the pore size distribution of the final product. The formation of channels through the templating of silicate clusters, though, did not substantially improve ion transport. Moreover, sacrificing microporous surfaces to create channels lowered the materials specific surface area, and the capacitance correspondingly decreased.

Tri-constituent coassembly between DPSD, F127 and TEOS yielded sol-gels that were subsequently dried, polymerized then carbonized. Although this synthesis resulted in a material with high surface area and high capacitance, a significant amount of that capacitance is irreversible and hence attributed to the psuedocapcitance of functional groups present. Non-rectangular CV curves confirm the functional groups' presence.

Since the CV plots of the weak acid catalyzed PdPHs- generated carbon are overwhelmingly rectangular and the material has good rate capability, this material was chosen among the others for further characterization.

The optimized carbon's porosity was characterized using nitrogen sorption. Type one isotherms with a large uptake step below a relative pressure of 0.2 indicate a mainly microporous material. The isotherms' lack of hysteresis suggests an open pore structure with uniform pore connectivity. Brunauer-Emmett-Teller (BET) surface area was calculated as 2275 m^2/g. The average pore width is 2.07 nm, while the majority of the pores are smaller than 2 nm.

Nitrogen sorption was also performed on the carbon-silicon composites. BET isotherms before and after etch are given in figure 2. The BET surface area before etch was 195 m^2/g, and was also centered around 2 nm. This confirms that most of this material's pores are generated from silicon removal. Pores present in the composites are attributed to voids developed by non crystalline stacking of the elastomers during polymerization.

Uniform micropores impart the material a high capacitance and good rate capability. The cyclic voltammogram at sweep rates between 2 and 100 mV/s in 1 M H_2SO_4 is shown in figure 3. At both negative and positive polarization through all sweep rates, the curves are symmetric and rectangular, indicating efficient ion transport. The curves' limited distortion illustrates the carbon's high rate capability. Figure 3b shows capacitance current at 0.4 V as a function of sweep rate. The linear trend in this plot confirms the material's high rate capability.

Most importantly, all materials produced had high and stable capacitance: At a 2mV/s sweep rate, a capacitance of 175 F/g is achieved in 1M H_2SO_4. As the sweep rate increases to 20 and 50 mV/s, the capacitance is reduced to 132 and 118 F/g, respectively. This good double layer capacitance is attributed to the material's conductivity, open pore structure and high surface area.

This capacitance is also on par with leading microporous carbon supercapacitor materials. For example, Liu et. al has reported a doped activated carbon based on polyaniline with capacitance at 2mV/s sweep of up to 235 F/g [1-14], however a major part of this high value is due to the psuedocapacitance of nitrogenated and oxygenated surface functionalities (Our sol-gel derived carbon that displays psuedocapacitance has similar values). Since our CV curves have a rectangular characteristic, the capacitance obtained isn't based on redox reaction but rather diffusion at the double layer, and hence is more stable with cycling.

Gryglewicz et. al prepared coal-based porous carbon using steam activation. After tuning activation parameters, they achieved a capacitance of 164 F/g in H2SO4 electrolyte [1-15]. By activating cresol-formaldehyde aerogels, Zhu et. al created supercapacitors with a maximum reported capacitance of 146 F/g in H2SO4 [1-16]. Commercial activated carbon frequently comes from organic sources such as coconut shells. Zhou, et. al reported typical coconut shell based activated carbon coin cell supecapacitors with a capacitace of 79 F/g in KOH [1-17]. Our materials outperform these activated carbons and have the advantage of more consistent synthesis from starting materials that lack significant variation.

These material's capacitances were also tested in 1M Net4BF4 in propylene carbonate. A capacitance of 60 F/g was reached at 2 mV/s. Since the operating window here was increased to -1.3 to 1.2 V compared to 0 to 1.0 volts in aqueous electrolyte, the energy density increased over tenfold in the organic system.

Certainly, such promising performance suggests the carbonization of elastomers as a novel, meaningful route towards microporous carbon, which is preferable to activation due to the precision with which the products' morphology can be controlled and is also preferable to carbide derivation of carbons due to the ease of synthesis.

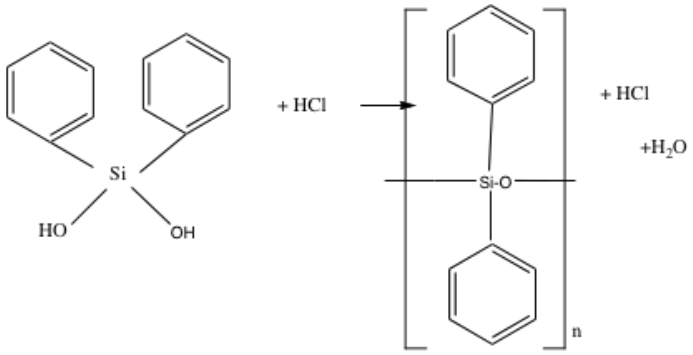

Figure 1-1: acid catalyzed condensation of DPSD into PdPhs

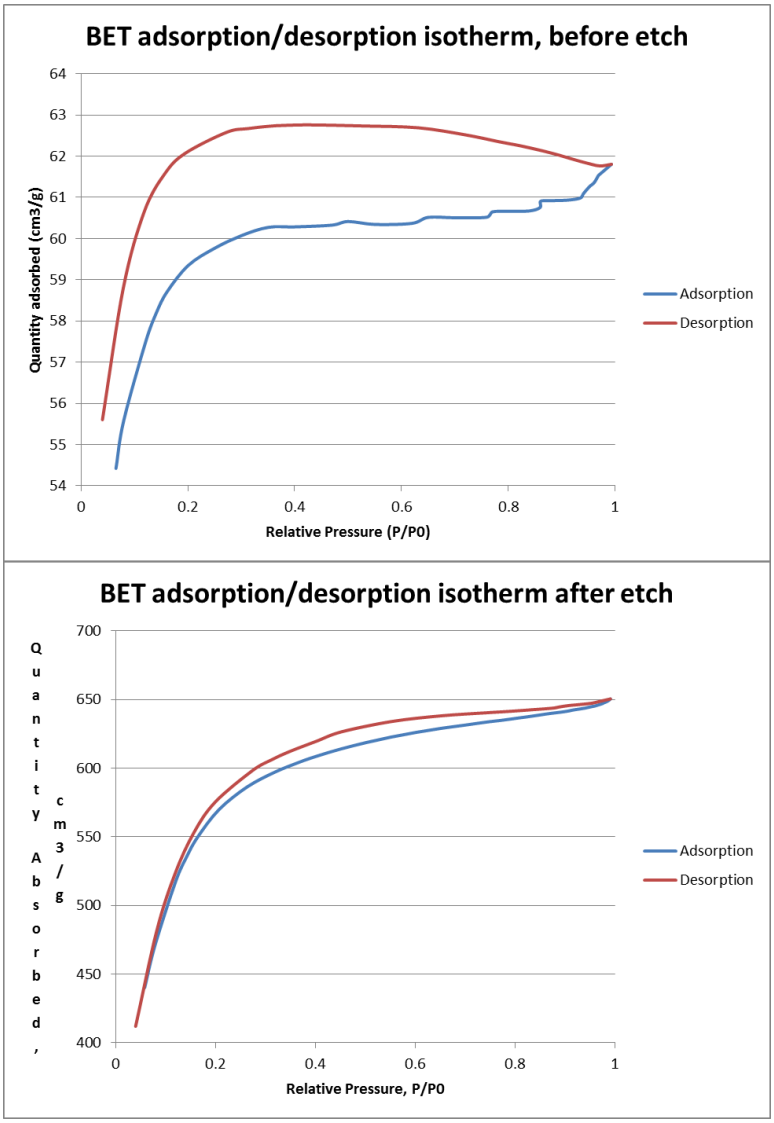

Figure 1-2: BET isotherms before and after etch

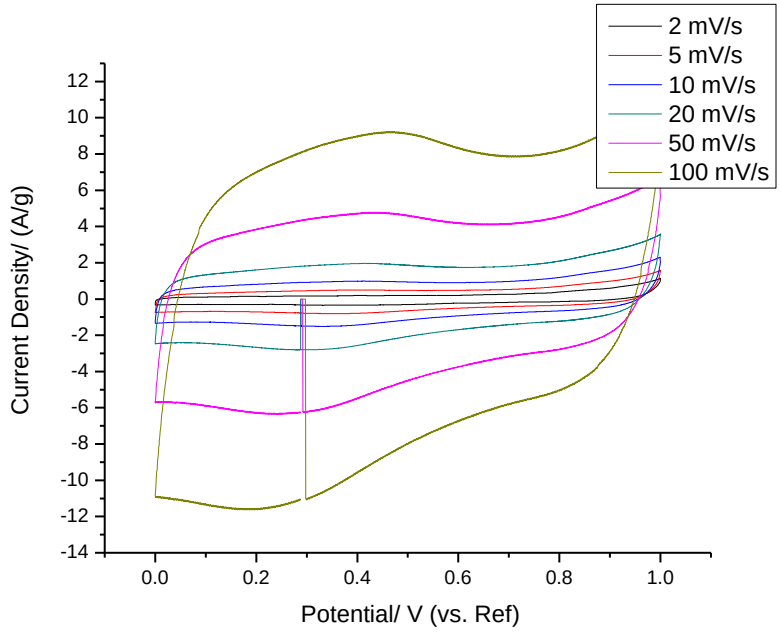

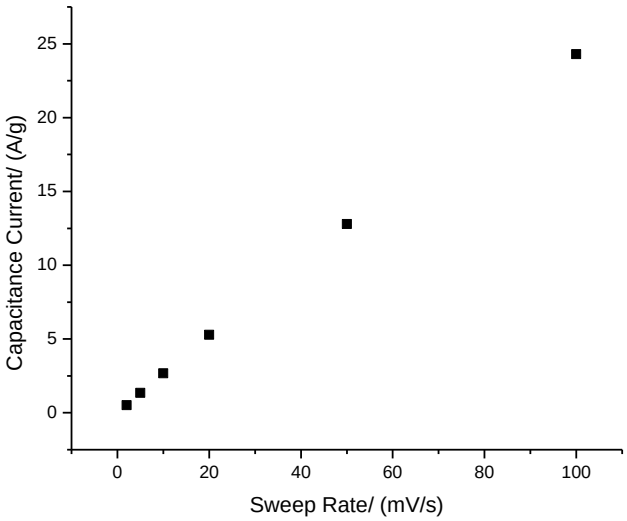

Figure 1-3: a. DPSD Cyclic voltammogram b. Capacitance current as a function of sweep rate

Experimental:

Synthesis: To synthesize this carbon, one mole part diphenylsilanediol (DPSD) is dissolved in dioxane and then condensed in the presence of 5- 10 mole parts water using .01 mole parts hydrochloric acid as catalyst. The condensation is let to proceed with stirring at room temperature for four hours. Then, the precursor mixture is poured into petri dishes and dried overnight, leaving opaque films of polydiphenylsiloxane (PdPhs). Films are further polymerized at 120˚ C in a vacuum oven. The sticky elastomers are then transferred into crucibles where they are carbonized in a nitrogen environment. To remove silicon, the black silicon/carbon composites are ground into fine powders then immersed in 12% HF for 12 hours. They are then rinsed profusely in deionized water and dried at 100˚ C for 24 hours under vacuum.

Characterization: Nitrogen sorption isotherms were measured using a Micromeritics ASAP 2020 (Micromeritics Instrument Corporation, Norcross, GA). Analysis was conducted at 77 K. Specific surface areas were calculated using the BET method with the adsorption branch relative pressure between 0.04 and 0.25. TEM images were obtained on a Philips CM120 operated at 120 kV (Philips/FEI Inc., Eindhoven, The Netherlands). X-ray diffraction measurements were conducted on a Panalytical X'Pert Pro X-ray powder diffractometer using Cu-K_α radiation (λ = 1.54 Å) with a current of 40 mA and 1° slit size and scanning from 2θ=10-80°.

Electrochemical Tests: Slurries of 80% microporous carbon, 10% poly(vinyledene) fluoride (PVDF) and 10% carbon black dispersed in N-methylpyrrolidinone (NMP) were

assembled, well mixed and coated onto titanium current collectors. Each electrode consisted of 0.5-1.5 mg active material. The electrodes were dried at 80˚ C under vacuum overnight and then assembled into half cells.

Half cells were assembled in a Princeton Applied Research model 263A potentiostat/galvanostat per the experimental schematic depicted in figure 4 and comprised a platinum counter electrode, a silver/silver chloride reference electrode housed in 3 M KCl and working electrodes as described above. Data was obtained through analog current sensors. All devices will were tested in 1M H_2SO_4 aqueous electrolyte.

Direct current cyclic voltammetry at a series of scan rates from 1mV/s to 50 mV/s was conducted from an 1.3 V to -1.2 V. Galvanostatic charge/discharge tests proceeded by charging and discharging the devices over 10^5 cycles.

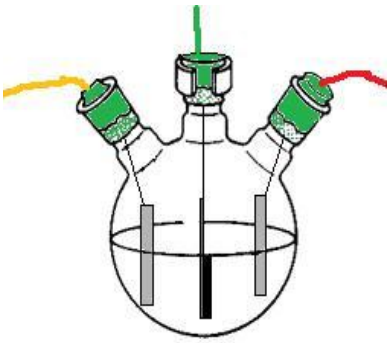

Figure 1-4: Electrochemical Cell Testing station schematic

References

1. Ortuzar, M; Moreno J. and Dixon, J., IEE Transactions on Industrial Electronics, v. 54, no 4, 2147-2156 (2007)

2.Galkin, I.; Stepanov, A. and Langis, J. Baltic Electronics Conference, 2006 International, pp.1-4, 2-4 Oct 2006

3.Lozano-Castello, D., Carlos Amoros, D., Linares-Solano, A., Shiraishi, S., Kurihara, H. and Oya, A. Carbon 41, 1765-1775 (2003)

4.Kötz, R. and Carlen, M. Electrochimica Acta 45, 2483-2498 (2000)

5.Frackowiak, E. and Béguin, F. Carbon 39, 937-950 (2001)

6.Vix-Guterl, C.; Frackowiak, E.; Jurewicz, K.; Friebe, M.; Parmentier, J.; and Beguin, F. Carbon 43, 1293-1302 (2005)

7.Chimola, J., Yushin, G., Gogotsi, Y., Portet, C., Simon, P. and Taberna, P.L. Science v.313 no 5794 pp 1760- 2763

8.Obreja, V.V.N., Physica E- Low Dimensional Systems of Nanostructures, v.40, no. 7, 2596-2605 (2008)

9. Jagtoyen, M., Derbyshire, F. Carbon, 27 p. 191 (1989)

10. H Benaddi, T.J Bandosz, J Jagiello, J.A Schwarz, J.N Rouzaud, D Legras, F Beguin. Carbon, v. 38 , p. 669 (2000)

11.W. Zhao, V. Fierro, C. Zlotea, E. Aylon, M.T. Izquierdo, M. Latroche *et al.* Int J Hydrogen Energy, 36 (18) pp. 11746–11751 (2011)

12. .Aurbach, D., Levi, M.D., Saltira, G., Levy, N., Pollak, E. and Muthu, J. J. Electrochem. Soc., Volume 155, Issue 10, pp. A745-A753 (2008)

13. Gogotsi, Y., Dash, R., Yushin, G., Yildirim, T., Laudisio, G. and Fischer, J. J Am Chem Soc. 127(46) 16006-16007 (2005)

14 .Liu, L., Liu, E., Li, J., Yang, Y., Shen, H., Huang, Z., Xiang, X. and Li, W. J. Power Sources v195 no5, 1516-1521 (2010)

15.Grylewicz, G., Machnikowski, J., Lorenc-Grabowska, E., Lota, G. and Frackowiak, E. Electrochimica Acta v. 50 no. 5, 1197-1206 (2005)

16. Zhu, Y., Hu, H., Li, W.C. and Zhang, X. J. Power Sources, v.62 no.1, 738-742 (2006)

17. .Zhou, P.W., Li, B.H., Kang, F.Y. and Zeng, Y.Q. New Carbon Materials v. 21, no.2, 125-131 (2006)

CHAPTER 2

High-Performance Supercapacitors Based on Hierarchically Porous Graphite Particles

Chapter 2 Statement of Contribution: This article was published in June 2011 in Advanced Energy Materials, volume one, pages 551-556 under the same title as this chapter and the author list is as follows: Zheng Chen, Jing Wen, Chunzhu Yan, Lynn Rice, Hiesang Sohn, Meiqing Shen, Mei Cai, Bruce Dunn, Yunfeng Lu. My contribution to this work was mainly in making the materials as a means of training and in helping the lead author "clean up" the language and structure of his manuscript.

Supercapacitors, a class of electrical-energy-storage devices with high power density (10^3–10^4 W kg^{-1}) and long cycling life (>100,000 cycles), hold great promise for a broad spectrum of applications, such as hybrid electric vehicles, power tools, and mobile electronic devices.[2-1, 2-2] However, current supercapacitors are still limited by their low energy density; improving the energy density while maintaining high power density is essential to realize the great potential of these devices. Since supercapacitors generally rely on electrical-double-layer capacitance or pseudocapacitance, to realize high energy density requires a sufficient number of ions to be absorbed on or inserted into the electrodes, while realizing high power density requires rapid transport of ions and electrons between the electrodes. To satisfy these criteria, the electrode materials should

exhibit high ion-storage density, excellent electronic conductivity, and effective ion-transport capability.

The current electrode materials used for supercapacitors are mainly activated carbons, carbon nanotubes (CNTs), and metal oxides. In this context, activated carbons possess high surface area, high microporosity, and moderate electronic conductivity. Capacitances up to 300 F g^{-1} in aqueous electrolytes or 120 F g^{-1} in organic electrolytes may be achieved at low discharge rates, which correspond to energy densities of ≈10 and 30 Wh kg^{-1}, respectively. At high discharge rates, however, their storage performance radically deteriorates due to the lagged ion transport within their tortuous microporous channels.[2-3] Carbon nanotubes (CNTs), on the other hand, possess excellent electronic conductivity and readily accessible external surfaces that can provide outstanding rate performance. However, CNTs generally have low surface areas, which provide low specific capacitances of less than 100 F g^{-1} in aqueous electrolytes or 50 F g^{-1} in organic electrolytes, respectively.[2-4–7] Alternatively, metal oxides, such as RuO_2,[2-8] MnO_2,[2-9] and V_2O_5 [2-10] may provide much higher pseudocapacitance through Faradaic reactions. Except the cost-prohibitive RuO_2, however, such materials are intrinsically poor ionic and electronic conductors, which limit their high-power application. Much effort has recently been devoted to making better electrode materials. For example, high-surface-area carbons with more regulated pore channels, such as carbide-derived carbon and zeolite-templated carbon, were synthesized with capacitances up to 150 F g^{-1} and improved high-rate performance in organic electrolytes,[2-11–13] however, their synthesis is extremely ineffective. Similarly, surface-functionalized CNTs may provide capacitances up to ≈150

F g^{-1} in H_2SO_4,[2-14] however, such modified CNTs are easily degraded during cycling. Up to now, making high-performance supercapacitor materials remains challenging. Herein, we report the design and fabrication of high-performance supercapacitors based on hierarchically porous graphite particles. As illustrated in Scheme 1, our supercapacitor electrodes are constructed from such particles containing interconnected micro-, meso-, and macropores. In comparison to the activated carbons with low rate capability, and CNTs with low capacitance, this unique structure provides the critical features required for high-performance electrodes: i) abundant micropores and mesopores provide the electrode with high surface areas, resulting in large capacitance and high energy density, ii) small particle size and hierarchically interconnected mesopores and macropores facilitate ion transport, which ensure high rate capability;[2-15, 16] iii) graphitized carbon provides excellent electronic conductivity that is another key factor for high rate capability; iv) carbon spheres can be densely packed into electrodes, which is important to ensure high volumetric energy density.

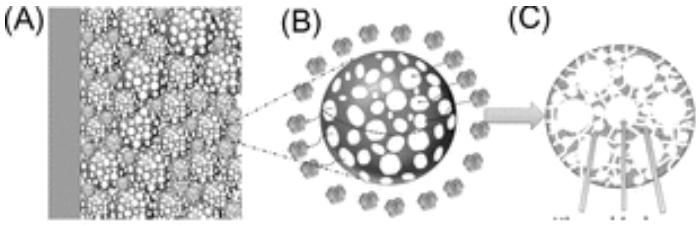

Scheme 2-1. Schematic of an electrode based on porous graphitized particles and its synthesis: A) An electrode made of densely packed carbon particles, B) schematic of a hierarchically porous carbon particle enabling effective transport of electrolyte ions, C)

cross-view of the carbon particles showing interconnected hierarchical porous structure, and D) an aerosol process used to synthesize the carbon particles.

The synthesis of such particles is based on a simple aerosol process.[2-17] As illustrated in Scheme 1, we started with aqueous solutions containing sucrose, nickel nitrate, colloidal silica particles (template for the mesopores), and silicate clusters (template for the micropores and mesopores); these underwent an atomization process using nitrogen as the carrier gas to form continuously generated aerosol droplets, which were passed through a heating zone and converted into nanocomposite particles. Subsequent carbonization in the presence of the nickel moieties in situ converted the sucrose into graphitized carbon. Further removal of the templates resulted in graphitized, porous carbon particles with high surface area and hierarchical pores. It is important to point out that such a continuous synthesis approach can be scaled up.

Figure 1 shows the representative scanning electron microscope (SEM) and transmission electron microscope (TEM) images of the aerosol-carbon particles. It is shown in Figure 1a that most of the particles are densely packed; the pressed pellets reached a density as high as 0.75 g cm^{-3}, which is much higher than those of commercial activated carbon with similar porosity (≈0.5 g cm^{-3}) and the CNTs used (0.56 g cm^{-3}). For device applications, to increase overall device capacitance, it is generally necessary to increase electrode porosity, which inevitably reduces the electrode density.[2-18] Therefore, a high gravimetric capacitance is often achieved by compromising rate capability and volumetric capacitance. The capability to synthesize high-surface-area carbon with high

packing density is therefore essential to ensure both high gravimetric and volumetric densities.

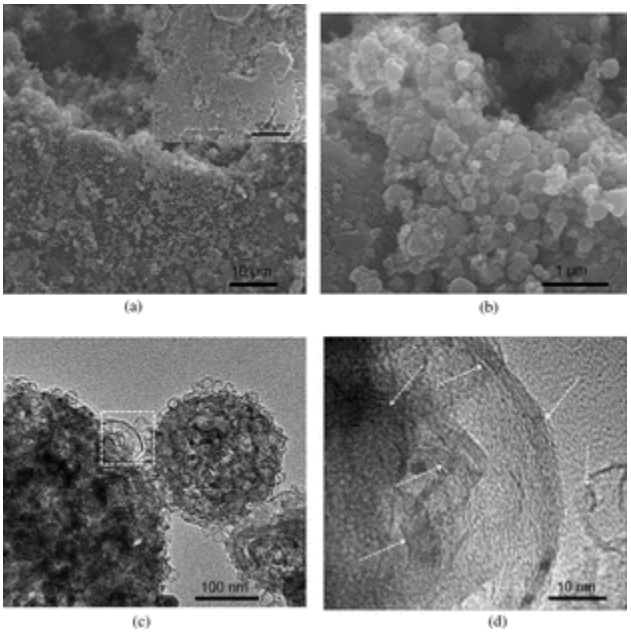

Figure 2-1. SEM and TEM images of the hierarchically porous aerosol-carbon particles: a) a low-magnification SEM image showing densely packed particles, b) a high-magnification SEM image showing spherical morphology with diameters ranging from 50–300 nm, c) a TEM image of the hierarchically porous aerosol-carbon particles, and d) high-magnification TEM showing the graphitized carbon structure.

High-magnification SEM shows that these particles are polydisperse with diameters ranging from 50 to 300 nm (Figure 1b), which are much smaller than that of the activated carbon normally used in commercial devices (5–20 μm). The TEM image (Figure 1c) reveals a highly porous sponge- or foamlike pore structure with interconnected mesopores and micropores. The diameters of the mesopores are around 10–20 nm, which

is consistent with the size of the colloidal silica template used (average diameter of 13 nm). The formation of micropores and smaller mesopores is due to the removal of silica clusters that were uniformly distributed within the carbon framework.[2-19]The high-resolution TEM (Figure 1d) image suggests that the "bubbles" observed in Figure 1c are graphite shells formed by the catalytic carbonization of sucrose.[2-20] The formation of such graphite shells, which improve the electrode conductivity, is further confirmed by their (002) graphite x-ray diffraction peak (Figure S1 in the Supporting Information).

Pore structure of the aerosol-carbon particles was investigated using nitrogen-sorption experiments. Figure2 shows nitrogen-sorption isotherms and pore-size distributions of the particles, which clearly suggest the coexistence of micropores and mesopores. The first nitrogen-uptake step, at a relative pressure below 0.2, is contributed by the micropores mainly templated from silica clusters. The second nitrogen-uptake step, at a relative pressure between 0.6 and 0.9, is attributed to the mesopores templated from colloidal silica particles. These mesopores are narrowly distributed and centred at 11 nm, which is consistent with the size of the colloidal silica template. These particles exhibit a high pore volume of 2.02 $cm^3\ g^{-1}$ and a Brunauer–Emmett–Teller (BET) surface area of 1522 $m^2\ g^{-1}$, of which ≈80% (1208 $m^2\ g^{-1}$) is contributed by the external surface, as calculated from the t-plot method. To better understand how such pore structure affects energy-storage performance, commercial activated carbon (AC) and multiwalled CNTs were also studied for comparison. As shown in Figure 2, the AC shows typical type I isotherms with uptake at low relative pressure, which suggests a microporous structure (pore diameter <2 nm) with an extremely high surface area of 2549 $m^2\ g^{-1}$ of which ≈64%

(1627 m^2 g^{-1}) is contributed by the external surface. As expected, the CNTs have quite limited surface area (156 m^2 g^{-1}) with some mesoporous structure resulting from stacking of the nanotubes. The external surface area (123 m^2 g^{-1}) accounts for ≈79% of the total CNTs' surface area.

Figure 2.-2 a) Nitrogen-sorption isotherms and b) pore-size distributions of the hierarchically porous aerosol-carbon particles (▲), AC (▪), and CNTs (•).

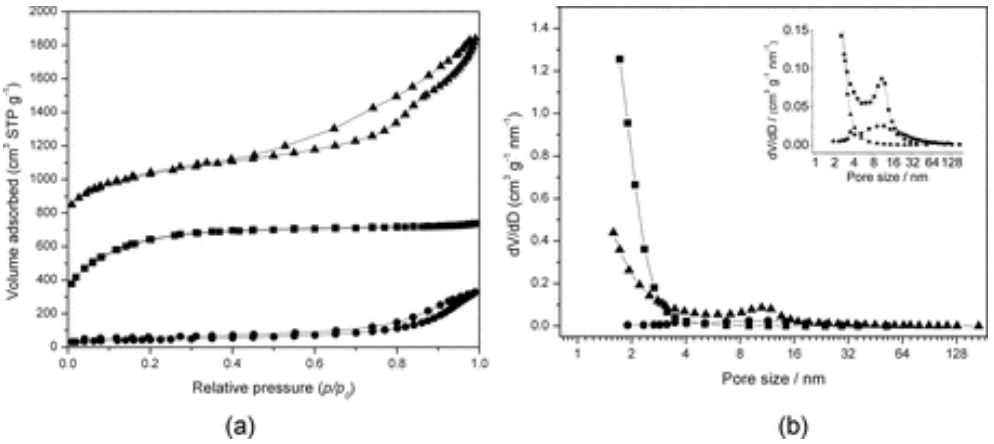

This unique hierarchical pore structure endows the particles with outstanding capacitive performance. Figure 3 compares cyclic-voltammetry (CV) plots of the aerosol-carbon particles, AC, and CNT electrodes at potential sweep rates of 5 (Figure 3a) and 50 mV s^{-1}(Figure 33b) in three-electrode cells using platinum foil as the counter electrode, silver wire as the quasi-reference electrode,[2-21] and 1 mNEt_4BF_4 in propylene carbonate (PC) as the electrolyte. At a potential sweep rate of 5 mV s^{-1}, all CV curves show typical capacitive behavior, as evidenced by their nearly rectangular voltammograms. For the AC electrode, the CV plot is fully developed at positive polarization, which is associated with solvated BF_4^- (1.35 nm)[2-21] adsorption. The CV plot shows obvious distortion at negative polarization, though, which is associated with adsorption of solvated NEt_4^+ (1.40

nm).[2-21] Generally, commercial activated carbons have abundantly irregular micropores and mesopores in the range of 0.3-4 nm with narrow bottlenecks that limit ion transport and adsorption. In addition, at sweep rates as low as 5 mV s^{-1}, ohmic drop across the electrode is not significant. Therefore, such an asymmetric CV characteristic could be attributable to a micropore size effect on the electrode kinetics, which has been recently confirmed on carbide-derived carbons in the same electrolyte system.[2-21] When potential sweep rates reach 50 mV s^{-1} (Figure 3b), CV plots of the AC electrode distort dramatically over the whole potential range. Such behavior can be ascribed to both the increased ohmic drop and the limited ion transport within their tortuous pore structure.

Figure 2-3. Cyclic voltammograms of various carbon electrodes at scan rate of a) 5 mV s^{-1} and b) 50 mV s^{-1}; c) capacitance current dependence on potential sweep rates at potential of –0.4 V (vs. reference electrode) and d) capacitance-frequency dependence of the aerosol-carbon particles (▲), AC (▪), and CNTs (•).

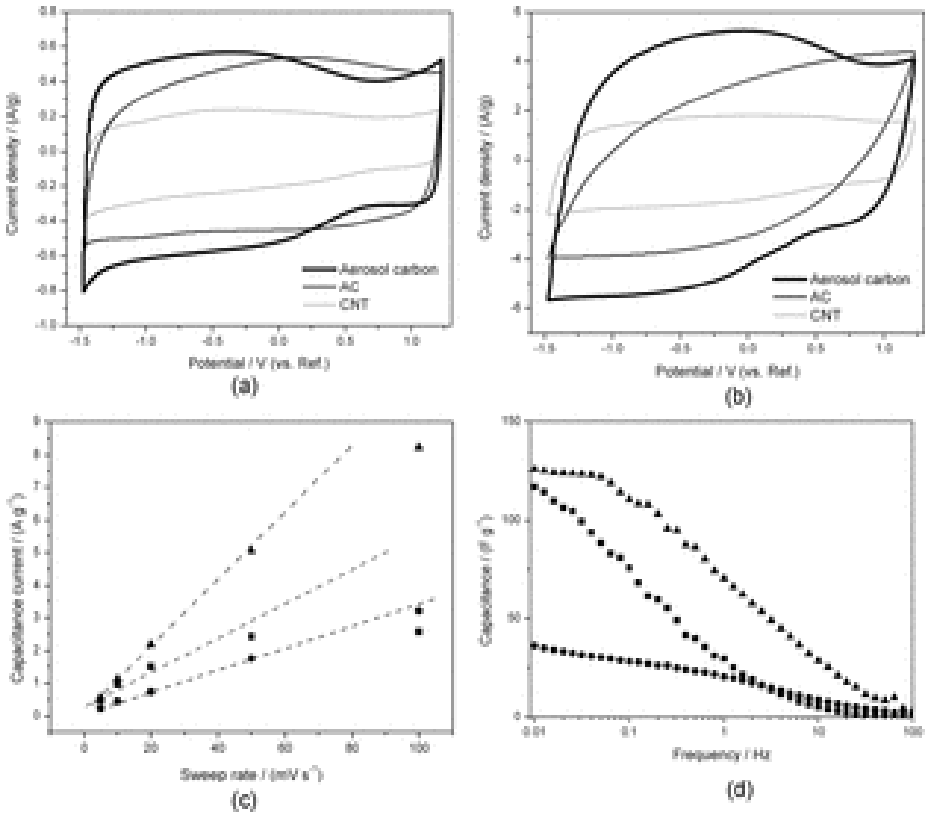

By comparison, at both potential sweep rates, the CV plots of the aerosol-carbon- and CNT-based electrodes show symmetric characteristics at both positive and negative polarizations, which suggests facile ion transport and good adsorption behavior. Although there are broad humps at potentials below 0.5 V on the CV curves of the aerosol-carbon electrodes, the charge and discharge processes are defined to not be limited by kinetics since the voltammetric response is very fast. Figure 3c shows the voltammetric current (i.e., the current value at a potential of –0.4 V) dependence on potential sweep rate. Unlike the AC electrodes, a perfect linear plot can be seen at sweep rates ranging from 5 to 50 mV s^{-1} for the aerosol-carbon electrodes, which confirms that their currents are purely capacitive in nature. Note that, due to the large ohmic drop, the current response at high sweep rate of 100 mV s^{-1} is nonlinear. This phenomenon was not observed for CNT

electrodes due to their better conductivity and lower porosity. For both the aerosol-carbon and CNT electrodes, only limited distortion of CV curves can be observed when the sweep rate increases from 5 to 100 mV s^{-1} (Figure S2), demonstrating very high rate-capability. We attribute this excellent capacitive performance to facile ion transport in the open pore structures and good electrode conductivity.

The facilitated ion-transport kinetics within hierarchical pore channels was further studied by electrochemical impedance spectroscopy (EIS). Figure 3d compares the capacitance dependence on frequency (10 mHz to 100 kHz) of each electrode. Clearly, the capacitance gradually decreases with increasing frequency, which is a common feature for porous carbon electrodes. The CNT electrodes exhibit slow capacitance drops due to fast ion transport and adsorption on their surface. Similarly, because of their open pore structure, the capacitance of aerosol-carbon electrodes approaches saturation at frequencies close to 0.1 Hz, which means that their ion adsorption can reach equilibrium in 10 s. By comparison, the AC electrodes show no sign of saturation at frequencies as low as 0.001 Hz, which indicates slow electrolyte-ion diffusion within their tortuous pore structure. Also, aerosol-carbon electrodes retain over 60% of their maximum capacitance at a frequency of 1 Hz, which is about three times higher than that of AC electrodes. This result further confirms the importance of creating easy ion-transport pathways in pursuit of high-rate supercapacitor electrodes.

To further quantify the specific capacitances of our aerosol-carbon-particles, galvanostatic charge/discharge tests were performed, and specific capacitances C_s (F g^{-1}) were calculated from the discharge curves of galvanostatic profiles. For example, as

shown in Figure4a, at a current density of 1 A g^{-1} the CNT-, AC-, and aerosol–carbon-based electrodes show capacitances of 34, 95, and 102 F g^{-1}, respectively. The aerosol-carbon electrodes display a more pronounced ohmic loss (IR drop) than the CNT electrodes, but their IR drop is much less than that of the AC electrodes. Calculated from the IR drop, the maximum power density of the aerosol–carbon electrodes (55 kW kg^{-1}) reaches ≈70% of the CNT electrode (78 kW kg^{-1}), which is 2.2 times that of the AC electrodes (25 kW kg^{-1}). Different current densities from 0.1 to 10 A g^{-1} were used to further investigate the rate capability (Figure 4b). The CNT electrodes retain ≈95% of their initial C_s (35 F g^{-1}) as current density increases from 0.1 to 10 A g^{-1}. Although they show a much higher C_s value of 106 F g^{-1} at a current density of 0.1 A g^{-1}, the AC electrodes have only 45% capacitance retention (50 F g^{-1}) at 10 A g^{-1}. By comparison, the aerosol-carbon electrodes have a high C_s value of 115 F g^{-1} at a current density of 0.1 A g^{-1}, and retain 83% of this capacitance (95 F g^{-1}) at 10 A g^{-1}, displaying excellent high-rate performance. Such capacitive performance is superior to the pore-opened single-walled CNTs with surface area of 2200 m^2 g^{-1}[2-22] and chemically modified graphene with surface area of 705 m^2 g^{-1}.[2-23] Note that recent carbide-derived carbon exhibits somewhat greater capacitances in acetonitrile, which has lower viscosity and a five times higher ionic conductivity than PC, and is an electrolyte solvent generally known to lead to higher capacitance.[2-22]

Figure 2-4. a) Constant current charge/discharge curves of different electrodes at current density of 1 A g^{-1}, b) specific capacitance as a function of current density, c) Ragone plots of various carbon electrodes (aerosol-carbon particles, AC, CNT, LN-porous

carbon, SK2200, Ness4600), and d) long-term cycling performance of symmetric supercapacitor made from aerosol-carbon particles.

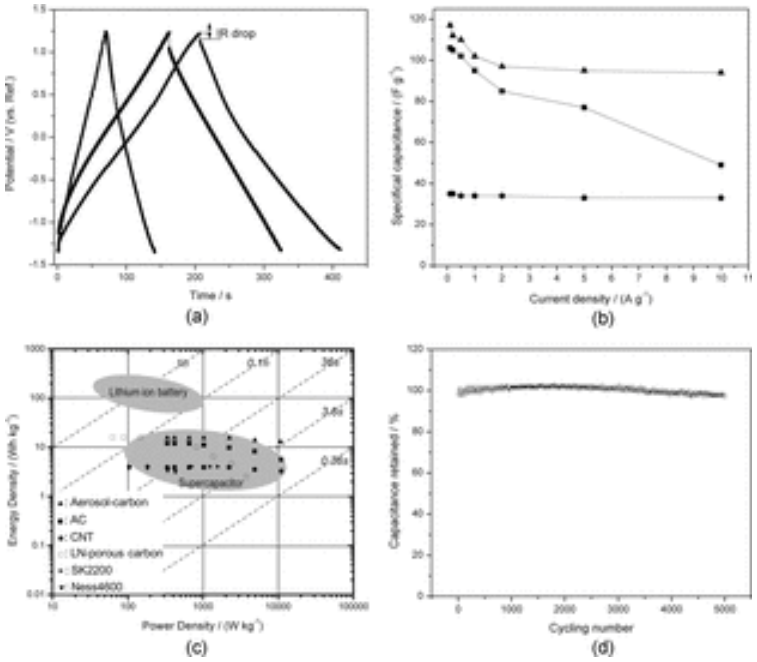

Consistent with electrochemical studies, these hierarchical aerosol–carbon particles exhibit outstanding device performance. In this work, symmetric supercapacitors were assembled to evaluate energy and power performance. The AC supercapacitor possesses a gravimetric energy density of 27 Wh kg^{-1} at a power output of 270 W kg^{-1} when only considering the mass of electrode-active materials, however, its energy density drops to 12 Wh kg^{-1} at a power density of 20 kW kg^{-1}. The CNT supercapacitor shows good rate capability but low energy density due to its low capacitance. In comparison, the aerosol-carbon supercapacitor reaches a gravimetric energy density of 30 Wh kg^{-1}at a power density of 270 W kg^{-1}, or 24 Wh kg^{-1} at 25 kW kg^{-1}. If considering the material density, our aerosol-carbon has a maximum volumetric energy density of 22.5 Wh L^{-1}, which is about twice of that of AC (13.5 Wh L^{-1}). Moreover, the device retains an energy density

of 18 Wh L^{-1} at 18.8 kW L^{-1}, which is significantly higher than that of AC (6 Wh L^{-1} at 10 kW L^{-1}). For better comparison, all the energy and power density are normalized to the mass of the whole device using a packaging factor of 0.4.[2-24] Figure 4c shows the Ragone plot, which displays the energy density dependence on the power output of various symmetric supercapacitors. The aerosol-carbon supercapacitor shows superior performance to that of the other devices. In particular, at 4 s of charge/discharge, the energy density of the aerosol-carbon supercapacitor is about two and three times higher than that of the AC and CNT supercapacitors, respectively. Compared with the state-of-the-art supercapacitors, our aerosol-carbon-based devices outperform many other prototypes and commercial devices, including those based on ACs, pore-opened CNTs,[2-22] LN-porous carbon,[2-25] SK2200,[2-26] and Ness4600.[2-26] Besides their high energy and high power performance, aerosol-carbon supercapacitors exhibit outstanding cycling stability. Figure 4d shows the results of long-term cycling tests at a current density of 2 A g^{-1}, which suggest a capacitance retention of ≈98% after 5000 cycles of charge and discharge.

In summary, we have synthesized a class of graphitized porous carbon particles using a continuous, scalable approach. Such carbon species contain a hierarchical pore structure and graphitized shells, providing a new material platform for high-performance supercapacitors with high packing density. This new family of porous carbon species could also be adapted for battery electrodes, fuel-cell catalyst supports, and other applications.

Experimental Section

Synthesis of Porous Graphitized Carbon Nanoparticles: For synthesis of the graphitized carbon particles, aqueous solutions containing deionized water (40 mL), sucrose (12 g), nickel (ii) nitrate hexahydrate (10 g), HCl (20 g, 0.1 m), and silicate templates including colloidal silica (20 g; AS 30%, Nissan Chemicals. Inc.) and tetraethylorthosilicate (TEOS; 16 g) were sent through an atomizer using nitrogen as a carrier gas. The atomizer dispersed the solution into aerosol droplets, which were then passed through a ceramic tube that was heated to 450 °C. Continuous solvent evaporation at the air/liquid interface of the aerosol droplets enriched the sucrose and silica, resulting in the formation of spherical silica/sucrose/nickel nanocomposite particles. The particles were then collected on a membrane filter in a press, and subsequent carbonization to 900 °C of the composite nanoparticles under N_2 atmosphere resulted in the formation of spherical silica/carbon/nickel composite nanoparticles. 1 m HCl and 5 m NaOH were used in sequence to remove the nickel and silica, respectively, to produce the porous carbon particles with graphitized shell structures.

AC and CNTs: Commercially available activated carbon (Yihuan Carbon Co., Ltd. Fuzhou, China) was used for comparison after vacuum-drying. Multiwalled CNTs were synthesized using a catalytic chemical-vapor deposition in a nanoagglomerate fluidized bed.[2-27] Before electrode fabrication, CNTs were functionalized by attaching carboxylic groups to the surface using a method similar to that developed by Gao et al.[2-28]

Characterization: Nitrogen-sorption isotherms were measured at 77 K with a Micromeritics ASAP 2020 analyzer (Micromeritics Instrument Corporation, Norcross,

GA). Specific surface areas (S_{BET}) were calculated by the BET method using the adsorption branch in a relative pressure range from 0.04–0.25. SEM experiments were conducted on a JEOL JSM-6700 FE-SEM (JEOL Ltd., Japan). TEM experiments were conducted on a Philips CM120 operated at 120 kV (Philips/FEI Inc., Eindhoven, The Netherlands).

Electrode Fabrication and Electrochemical Measurements: The aerosol-carbon particles, AC, and CNTs were assembled onto nickel-foam current collectors. Briefly, 85% of the electrochemically active material, 5% carbon black, and 10% poly(vinylidene fluoride) (PVDF) dispersed in N-methylpyrrolidinone (NMP) were mixed to form slurries. The homogenous slurries were coated onto nickel-foam substrates and dried at 80 °C for 10 min under vacuum. As-formed electrodes were then pressed at a pressure of 2 MPa and further dried under vacuum at 100 °C for another 12 h. Electrodes were obtained by coating an active mass of ≈1–3 mg onto each current collector (0.5 × 0.5 cm).

The electrochemical measurements were carried out on a Solartron 1860/1287 Electrochemical Interface (Solartron Analytical, Oak Ridge, TN). The electrolyte solution was a 1 m tetraethylammonium tetrafluoroborate (NEt_4BF_4) in PC solution and platinum foil was used as the counter electrode. Silver wire was used as a quasi-reference electrode. CV measurements were carried out in an argon-filled glove box using cut-off voltages of –1.5 and 1.2 V versus Ag. The specific capacitance, C_s (F g^{-1}) of the electrode materials was calculated from the discharge curve of galvanostatic cycles, according to $C = I/(dV/dt) \approx I/(\Delta V/\Delta t)$, where I is the constant discharge current density, E is the cell voltage, and dV/dt is the slope of the discharge curve. The EIS tests

were operated in the frequency range of 10 mHz–100 kHz with 10 mV AC amplitude. The gravimetric capacitance, C, was also calculated according to $C = 1/[2\pi f\, Im(Z)M]$, where f is the operating frequency (Hz), Im(Z) is the imaginary part of the electrode resistance (ohm), and M (g) is the mass of the electrode.

To make 2032-type coin cells, glass fiber (GF/D) from Whatman was used as a separator. The cells were assembled in a glove-box under an argon atmosphere. Charge and discharge measurements and long-term cycling tests were carried out by LAND CT2000 (Wuhan Jinnuo Electronics, Ltd., Wuhan, China) at different current densities. Symmetric cells were charged and discharged between 2.7 and 0 V. The specific capacitance, and power and energy density were calculated based on the total mass or volume of anode and cathode materials. Energy density was calculated using $E = 1/2\ CV^2$, where C is the total cell capacitance and V is the cell-operation potential. The maximum power density was calculated using $P_{max} = V^2/(4ESR*M)$, where ESR is the equivalent series resistance and M (g) is the total mass of anode and cathode materials.

Acknowledgements

This work was partially supported by General Motor Inc. (M. C. and Y. L.) and the Center for Molecularly Assembled Material Architectures for Solar Energy Production, Storage and Carbon Capture, an Energy Frontier Research Center funded by the U.S. Department of Energy, Office of Science, and Office of Basic Energy Sciences under award DE-SC0001342 (B.D. and Y. L.). We also acknowledge the support from IMRA America.

1. P. Simon, Y. Gogotsi, Nat. Mater. 2008, 7, 845.
2. J. R. Miller, A. F. Burke, Electrochem. Soc. Interface. 2008, 17, 53.
3. E. Frackowiak, Phys. Chem. Chem. Phys. 2007, 9, 1774.
4. C. M. Niu, E. K. Sichel, R. Hoch, D. Moy, H. Tennent, Appl. Phys. Lett. 1997, 70, 1480.
5. M. Kaempgen, J. Ma, G. Gruner, G. Wee, S. G. Mhaisalkar, Appl. Phys. Lett. 2007, 90, 264104.
6. C. S. Du, N. Pan, Nanotechnology 2006, 17, 5314.
7. M. Kaempgen, C. K. Chan, J. Ma, Y. Cui, G. Gruner, Nano Lett. 2009, 9, 1872.
8. J. P. Zheng, P. J. Cygan, T. R. Jow, J. Electrochem. Soc. 1995, 142, 5.
9. M. Toupin, T. Brousse, D. Belanger, Chem. Mater. 2002, 14, 3946.
10. Z. Chen, Y. C. Qin, D. Weng, Q. F. Xiao, Y. T. Peng, X. L. Wang, H. X. Li, F. Wei, Y. F. Lu, Adv. Funct. Mater. 2009, 19, 3420.
11. Direct Link:
12. J. Chmiola, G. Yushin, Y. Gogotsi, C. Portet, P. Simon, P. L. Taberna, Science 2006, 313, 1760.
13. H. Itoi, H. Nishihara, T. Kogure, T. Kyotani, J. Am. Chem. Soc. 2011, 133, 1165.
14. S. W. Lee, B. S. Kim, S. Chen, Y. Shao-Horn, P. T. Hammond, J. Am. Chem. Soc. 2009, 131, 671.
15. D. W. Wang, F. Li, M. Liu, G. Q. Lu, H. M. Cheng, Angew. Chem. Int. Ed. 2008, 47, 373.

16. C. Portet, G. Yushin, Y. Gogotsi, J. Electrochem. Soc. 2008, 155, A531.
17. J. E. Hampsey, Q. Hu, L. Rice, J. Pang, Z. Wu, Y. Lu, Chem. Comm. 2005, 28, 3606.
18. C. Portet, M. A. Lillo-Rodenas, A. Linares-Solano, Y. Gogotsi, Phys. Chem. Chem. Phys. 2009, 11, 4943.
19. J. B. Pang, Q. Y. Hu, Z. W. Wu, J. E. Hampsey, J. B He Y. F. Lu, Microporous Mesoporous Mater. 2004, 74, 6.
20. H. S. Bengaard, J. K. Nørskov, J. Sehested, B. S. Clausen, L. P. Nielsen, A. M. Molenbroek, J. R. Rostrup-Nielsen, J. Catal.2002, 209, 365.
21. R. Lin, P. L. Taberna, J. Chmiola, D. Guay, Y. Gogotsi, P. Simon, J. Electrochem. Soc. 2009, 156, A7.
22. T. Hiraoka, A. Izadi-Najafabadi, T. Yamada, D. N. Futaba, S. Yasuda, O. Tanaike, H. Hatori, M. Yumura, S. lijima, K. Hata,Adv. Funct. Mater. 2010, 20, 422.
23. M. D. Stoller, S. Park, Y. Zhu, J. An, R. S. Ruoff, Nano Lett. 2008, 8, 3498.
24. Z. Chen, V. Augustyn, J. Wen, Y. Zhang, M. Shen, B. Dunn, Y. Lu, Adv. Mater. 2011, 23, 791.
25. Direct Link:
26. E. Raymundo-Piñero, M. Cadek, F. Beguin, Adv. Funct. Mater. 2009, 19, 1032.
27. Direct Link:

A. Burke, Proc. IEEE Veh. Power Propulsion Conf. (VPPC”05), 2005, 356.

28. F. Wei, Q. Zhang, W. Z. Qian, H. Yu, Y. Wang, G. H. Luo, G. H. Xu, D. Z. Wang, Powder Technol. 2008, 183, 10.

29. C. Gao, C. D. Vo, Y. Z. Jin, W. W. Li, S. P. Armes, Macromolecules 2005, 38, 8634.

CHAPTER 3

High-performance flexible lithium-ion electrodes based on robust network architecture

Chapter 3 statement of contribution: This article was published in February 2012 in Energy & Environmental Science, volume five pages 6845-6849 under the same title as this chapter and the author list is as follows: Xilai Jia, Zheng Chen, Arnold Suwarnasarn , Lynn Rice, Xiaolei Wang , Hiesang Sohn , Qiang Zhang, Benjamin M. Wu, Fei Wei and Yunfeng Lu.

My contribution to this work was, like that of chapter two, in materials synthesis and helping the lead author polish the language and structure of his manuscript. The lead author provided me a tremendous source of support and inspiration in daily discussions, and I hope that, at times, my questions or suggestions were likewise useful to him.

Abstract

Highly robust, flexible, binder-free lithium-ion electrodes were fabricated based on interpenetrative nanocomposites of ultra-long CNTs and V_2O_5 nanowires. Such robust composite-network architecture provides the electrodes with effective charge transport and structural integrity, leading to high-performance flexible electrodes with high capacity, high rate-capability and excellent cycling stability.

Broader context

Flexible, lightweight energy-storage devices are of great interest for wearable devices, rollup displays, portable gadgets and other applications. To realize the great potential, one paramount challenge is the ability of making flexible electrodes with robust mechanical property and excellent electrochemical performance. However, current approaches for fabricating high-performance flexible electrodes are still ineffective enough, which often leads to poor electrode performance. Herein, we demonstrate effective design and fabrication of highly robust, flexible, and binder-free lithium-ion electrodes based on interpenetrative nanocomposites of ultra-long CNTs and V_2O_5 nanowires. Such robust composite-network architecture enables effective charge transport and electrode integrity, thus endowing the electrodes with high capacity, high rate-capability and excellent cycling stability. This work provides a simple but effective strategy to fabricate flexible energy-storage devices.

Introduction

Flexible, lightweight energy-storage devices (batteries and supercapacitors) are of great interest for wearable devices, rollup displays, portable gadgets and other applications.[3-1,2] To convert such potentials into reality, one paramount challenge is the ability of making flexible electrodes with robust mechanical property and excellent electrochemical performance. To date, the most common approach for fabricating flexible electrodes is directly coating slurries containing electrode active materials, carbon and binder on flexible substrates such as plastic[3-1,3,4] or paper.[3-5,6] Such an approach, though, utilizes a substantial amount of inert components that inevitably

compromise device energy density. As an alternative approach, flexible electrodes were fabricated from conducting polymers, such as polyaniline, polypyrrole and their derivatives;[3-7,8] however, such electrodes are brittle with low capacity (<150 mA h g^{-1}) and poor stability. Integrating conducting polymers with carbon nanotubes (CNTs)[3-9,10] or graphene[3-11] can improve the stability and flexibility but lead to decreased capacity. Herein, we report a class of high-performance flexible electrodes based on composited networks of ultra-long CNTs and vanadium oxide (V_2O_5) nanowires, a high-energy material with a capacity of ~300 mA h g^{-1} based on two-lithium intercalation. As illustrated in Fig.1, we started with networks of CNTs dispersed in a precursor solution of nanowires; an in situ hydrothermal reaction created three-dimensional (3-D) nanowire networks within the CNT networks, leading to the formation of CNT/nanowire composite gels with an interpenetrating network structure. Subsequent filtration condensed the networks into highly robust and flexible freestanding composite electrodes. Such a unique network structure provides critical features required for high-performance flexible electrodes: (i) the CNT scaffold provides fast electron transport pathways while the nanowire scaffold provides high charge-storage capacity with shortened lithium diffusion length; (ii) the network structure creates interconnected channels for effective ion transport; and (iii) the interpenetrating network of ultra-long CNTs and nanowires synergistically provides excellent mechanical robustness and high-rate lithium storage performance.

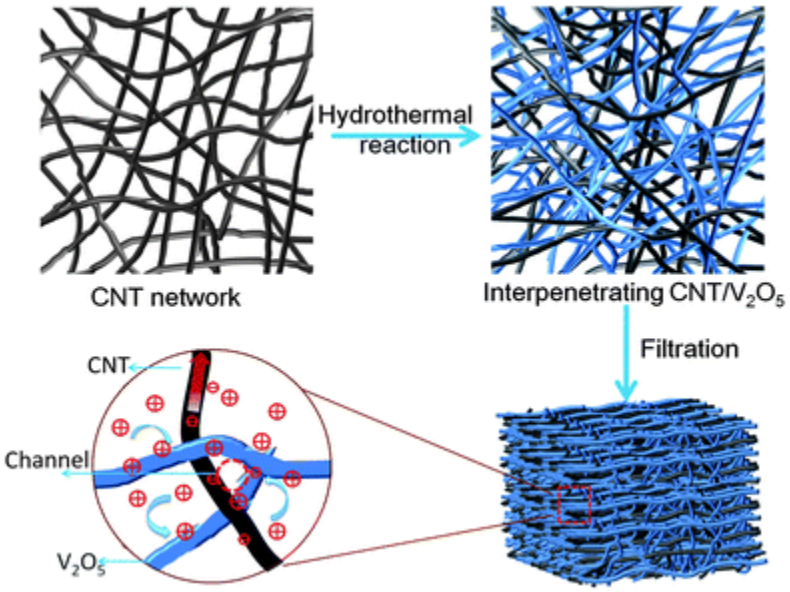

Fig. 3-1 Schematic of synthesis of the nanocomposites of ultra-long CNTs and V_2O_5 nanowires with an interpenetrative network structure.

Note that flexible electrodes have been fabricated by depositing thin layers of V_2O_5 onto graphene paper with outstanding electrochemical performance; such electrodes, however, exhibit rather low capacity due to low V_2O_5 loading.[3-12] Similarly, flexible electrodes have been made from thin composites of In_2O_3 nanowires and CNTs but with extremely low In_2O_3 loading (<0.01 mg cm^{-2}).[3-13] Recently, flexible electrodes were reported by a simple physical mixing of CNTs with V_2O_5 nanowires; to achieve a moderate stability, the discharge cut-off potential was set to be rather high (e.g. 2.5 V vs. Li^+/Li),[3-14] leading to low capacity. Making V_2O_5 nanowire/graphene composites resulted in much improved capacity but unsatisfactory stability down to a low potential (1.5 V vs. Li^+/Li).[3-15] Strikingly, the robust mechanical property of such CNT/nanowire composites endows their corresponding bulk electrodes with high capacity, high rate and

excellent stability down to a moderate potential (1.8 V vs. Li^+/Li). This work provides a simple but effective fabrication strategy towards making better flexible lithium-ion electrodes.

Experimental

Synthesis of the CNT/V_2O_5 composites

The ultra-long CNT arrays were prepared by the floating chemical vapor deposition (CVD) method.[3-16,17] Pristine CNTs were added into a cylinder by gas shearing to make ultra-long CNT aerogels.[3-18] Then the aerogels were immersed in 3 mol L^{-1} HCl solution to remove the residual catalyst impurities. The ultra-long CNTs were dried in a vacuum oven for 24 h at 120 °C. The structure of CNTs was characterized by scanning electron microscope (SEM) and transmission electron microscopy (TEM), as shown in Fig. S1†. An in situ hydrothermal method was used to synthesize the composites as described previously.[3-19] Briefly, appropriate amounts of the ultra-long CNT aerogels, HCl (2 M, 0.5 mL), ammonium metavanadate (NH_4VO_3, 0.15 g), surfactant P123 ($EO_{20}PO_{70}EO_{20}$, where EO and PO are ethylene oxide and propylene oxide, respectively, 0.25 g) and 15 mL of de-ionized water were mixed and stirred for 24 h. Then, the mixtures were transferred to 20 mL Teflon-lined autoclaves, heated to 120 °C and kept for 24 h in an oven. The resulting precipitates were filtered and washed with water and acetone several times then dried under vacuum at 120 °C for 24 h. The amounts of CNTs in the precursors were adjusted to 0.006, 0.020, 0.037, 0.005 and 0.075 g to obtain nanocomposites with CNT contents of 6, 15, 25, 30 and 40 wt%, respectively.

CNT/V_2O_5 nanowire composites were also made using short CNTs with acid treatment.[3-19] Pure V_2O_5 nanowires were synthesized under the same conditions without adding CNTs.

Material and electrode characterizations

X-Ray diffraction was conducted on a Panalytical X'Pert Pro X-ray powder diffractometer using Cu-K_α radiation (λ = 1.54 Å). Nitrogen sorption isotherms were measured at 77 K with a Micromeritics ASAP 2020 analyzer. The specific surface areas (S_{BET}) were calculated by the Brunauer–Emmett–Teller (BET) method using an adsorption branch in a relative pressure range from 0.04 to 0.25. The pore size distributions (D_p) were derived from the adsorption branch of isotherms using the Barrett–Joyner–Halenda (BJH) model. SEM experiments were conducted on a JEOL JSM-6700 FE-SEM. TEM experiments were conducted on a Philips CM120 instrument operated at 120 kV. Mechanical tests were conducted on an INSTRON 5564 with a speed of 2.0 mm min^{-1} at room temperature. Details of the mechanical tests are provided as ESI (Fig. S2†). For the electrochemical test, the free-standing composite films were cut into desired sizes to make electrodes. The electrolyte solution was a 1 M $LiClO_4$ in propylene carbonate (PC) and lithium foils were used as both the counter and reference electrodes. The CV and EIS measurements were carried out on a Solartron 1860/1287 Electrochemical Interface. To make 2032-type coin cells, glass fiber (GF/D) papers from Whatman were used as the separators. Both the three-electrode cell test and coin cell assembly were conducted in an argon-filled glove box. The galvanostatic

charge/discharge measurements were carried out by a LAND CT2000 battery tester at different rates.

Results and discussion

Fig. 2a shows a representative SEM image of a nanocomposite gel (25 wt% of CNTs), exhibiting a uniform nanowire network. Ultra-long CNTs are clearly observed interpenetrating through the nanowire network. The nanowires with diameters of 30–50 nm branch out and form a 3-D network structure. Microscopically, each nanowire has an ordered layered structure as evidenced from the selective area electron diffraction (SAED) (Fig. S3†) and X-ray diffraction patterns (Fig. S4†). Fig. 2b shows a digital photograph (inset) and SEM image of a flexible electrode with a fibrous network structure. Such a composite network structure creates interconnected pores and has a surface area of ~80 $m^2 g^{-1}$ and a broad pore size distribution from 6–30 nm (Fig. S5†).

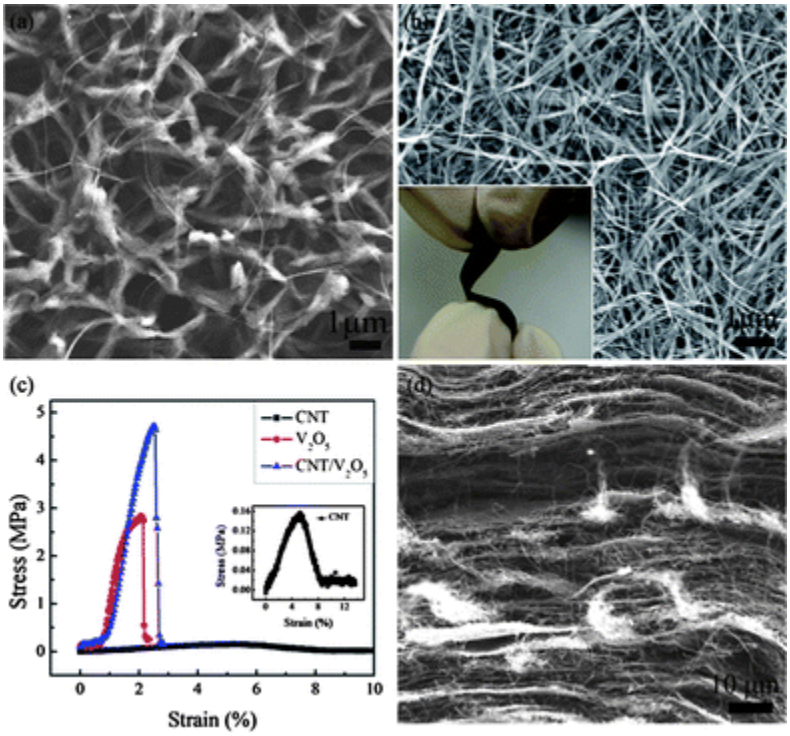

Fig. 3-2 (a) SEM image of V_2O_5 nanowire networks and CNTs penetrating through the networks. (b) SEM image of an electrode surface and a digital photograph of a flexible electrode with a dimension of 1 cm × 3 cm × 130 μm (inset). (c) Stress–strain curves of free-standing electrodes of CNTs, pure V_2O_5 nanowires, and CNT/V_2O_5 composites. (d) Cross-sectional SEM image of the CNT/V_2O_5composite electrode.

Such a unique network structure endows the flexible electrodes with excellent mechanical robustness. Fig. 2c compares the stress–strain curves of electrodes based on nanowires, CNTs, and CNT/nanowire composites. As expected, the nanowire electrode is brittle with a breaking strain of 2.1% and strength of 2.8 MPa. The CNT electrode, on the other hand, shows a much lower strength of 0.16 MPa but a larger strain of 8.0%. The CNT/nanowire composite electrode shows a strength of 4.7 MPa, which is significantly

higher than that of CNT and nanowire electrodes. The breaking strain of the composite electrode (2.8%) is only slightly higher than that of the nanowire electrode. The toughness of the nanocomposite (5.1×10^4 J m^{-3}), though, is almost twice that of the pure nanowire electrode (2.9×10^4 J m^{-3}) (Fig. S2†). Accordingly, the nanocomposite possesses an average modulus of 290 MPa, close to that of commercial paper. By comparison, flexible electrodes reported so far are still not strong enough to endure mechanical testing. To our knowledge, the strength of our nanocomposites exceeds that of all the other free-standing flexible electrodes and approaches that of many CNT sheets.[3-20]

Fig. 2d shows a cross-sectional SEM image of the ruptured surface of the nanocomposite electrode, revealing a unique multilayered structure. It was also found that the CNTs and nanowires are interconnected within these layers, which were stretched out from their entangled networks during the mechanical testing. Remarkably, removing V_2O_5 nanowires from the composite films using 37 wt% HCl resulted in CNT sheets that maintained the network integrity (Fig. S6†). We believe that the significantly enhanced mechanical performance of the composite electrodes is attributed synergistically to the interpenetrating structure between the ultra-long CNTs and V_2O_5 nanowires, which helps to absorb energy and accommodate mechanical stress during stretching.[3-21] The formation of a layered structure may be ascribed to the high aspect ratio of ultra-long CNTs, which are readily aligned during vacuum filtration.[3-20] In contrast, nanocomposites made from short CNTs do not show such a layered structure (Fig. S7†). We expect that the mechanical performance of the nanocomposites can be further enhanced by tuning

CNT/nanowire compositions as well as their interface. Systematic studies to further improve mechanical performance are underway.

The robust structure endows CNT/V_2O_5 nanocomposite electrodes with excellent lithium storage capability, which was examined using various electrochemical tests. Cyclic voltammetry (CV) was first conducted to investigate their lithium storage behavior. In these studies, three-electrode cells using 1 M $LiClO_4$ in a propylene carbonate (PC) electrolyte were used. The voltage window was 1.8 to 4.0 V (vs. Li/Li^+). V_2O_5 nanowires present a typical layered structure that can host a large amount of lithium ions. During the discharge process, which is accompanied by an electrochemical reduction, lithium ions are inserted mainly within the layers. While the charge process involves an electrochemical oxidation and lithium-ion extraction. More specifically, such electrochemical Li^+ insertion/extraction occurring can be expressed as $V_2O_5 + xLi^+ + xe^- \leftrightarrow Li_xV_2O_5$, where x is the mole fraction of inserted lithium ions. Fig. 3a compares the CV curves of a pure V_2O_5 nanowire electrode, a pure ultra-long CNT electrode, and a CNT/V_2O_5 (containing 25 wt% CNTs) nanocomposite electrode. The V_2O_5 nanowire electrode shows a pair of broad, asymmetric redox peaks, especially for the cathodic scan, indicating sluggish lithium ion insertion/extraction kinetics. In contrast, the nanocomposite electrode shows two pairs of well-defined redox peaks. The cathodic peaks at 2.3 and 2.7 V represent the lithium insertion from two different energy sites and correspond to the lithium extraction at 2.4 and 2.9 V by the anodic process, respectively, suggesting reversible charge/discharge processes. The improved electrode kinetics in the nanocomposite electrode is associated with improved transport in the

hierarchical porous structure of the electrodes and, more importantly, increased conductivity due to the presence of an ultra-long CNT network. The pure CNT electrode shows a featureless CV curve with low capacitance due to the nature of electrical double layer capacitance; therefore, the capacitive contribution of CNTs within the composite electrode is relatively small compared to that of the nanowires.

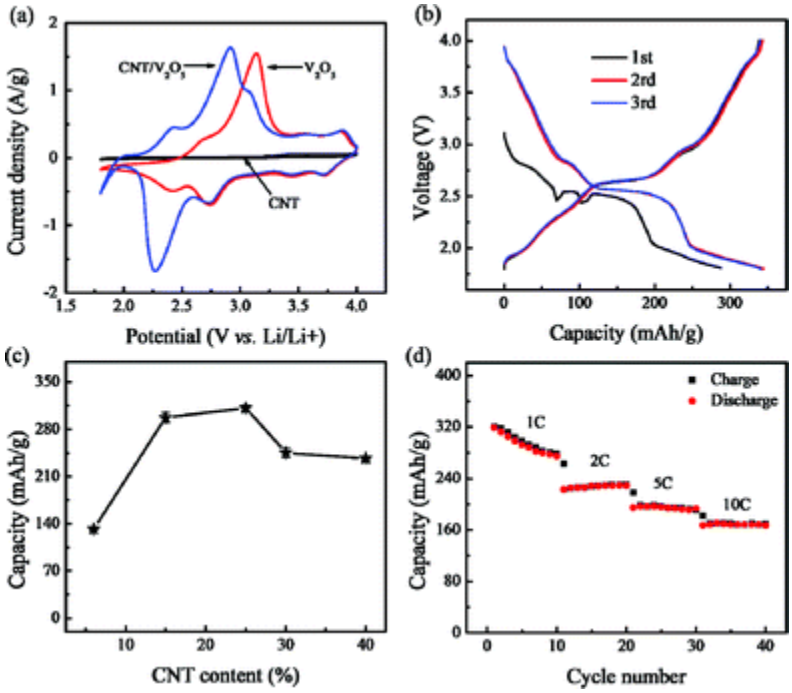

Fig. 3-3 (a) CV curves of CNT, V_2O_5, and CNT/V_2O_5 electrodes at a voltage range of 1.8 to 4 V (vs. Li/Li^+) at a potential scan rate of 1.0 mV s^{-1}. (b) First three charge/discharge cycles of a CNT/V_2O_5 nanocomposite electrode (containing 25 wt% CNTs) with a thickness of ~30 μm. (c) Dependence of lithium-storage capacity on the CNT content in composites. The current density was 70 mA g^{-1} and the capacity was calculated based on the mass of whole electrode. (d) Rate performance of the CNT/V_2O_5 cathode.

To further quantify the lithium storage capability, galvanostatic charge/discharge was conducted using coin-cells where lithium discs were used as the negative electrodes. Fig. 3b shows the charge/discharge profiles of the CNT/V_2O_5 electrodes (25 wt% CNTs) at a current density of 70 mA g^{-1} between 1.8 and 4.0 V (vs. Li/Li^+). The lithium insertion during the first cycle is different from those observed in subsequent cycles due to the initial complex formation process. From the second cycle, however, the charge/discharge process becomes stable. Three obvious plateaus at 3.8, 2.8, and 2.5 V are observed in the discharge curves, suggesting structure transition of V_2O_5 during the lithium-insertion process, which is similar to that of pure V_2O_5 electrodes and is consistent with previous reports.[3-22,23] The discharge capacity of the composite electrodes reaches up to 340 mA h g^{-1}, which exceeds that of the pure V_2O_5 nanowire electrodes (<100 mA h g^{-1}) and most nanostructured V_2O_5 electrodes reported so far.[3-14,22–27] Such an electrode still presents a capacity of over 260 mA h g^{-1}after 50 cycles at the charge/discharge rate of 0.25 C, suggesting good electrode stability (Fig. S8†).

To study the synergic effects between the conductive CNTs and high-capacity V_2O_5 nanowires, CNT/V_2O_5 composite electrodes (~30 μm thick) with various CNT compositions were examined. Fig. 3c shows their overall capacities vs. CNT content at a current density of 70 mA g^{-1}. The CNT/V_2O_5 electrodes with 6, 15, 25, 30 and 40 wt% loading of CNTs deliver reversible capacities of 130, 308, 318, 257 and 240 mA h g^{-1}, respectively. The composite electrodes with low CNT content (6 wt%) deliver low capacity due to inefficient electron transfer; alternatively, the composite electrodes with low V_2O_5 content (60 wt%) also show low capacity due to insufficient active material

loading. A high discharge capacity is achieved at 25 wt% CNT loading, which is significantly higher than the sum of contributions from the CNT and nanowire constituents. A similar synergic effect was also observed in the aqueous electrolyte and other nanocomposite systems.[3-19,28]

Besides their high capacity, our robust composite electrodes also exhibit excellent rate-capability. Fig. 3d shows the rate performance of the composite electrode (25 wt% CNTs and with a thickness of ~30 μm). At a charge/discharge rate of 1 C (280 mA g^{-1}; 1 C corresponds to a full charge or discharge in 1 h), a capacity of 318 mA h g^{-1} is realized. At 2 C, though the capacity drops to 275 mA h g^{-1} after 10 cycles, it remains stable with a value of ~230 mA h g^{-1} thereafter. Even at very high rates, such as 5 C and 10 C, the electrode retains a capacity of 197 and 169 mA h g^{-1}, respectively. Note that such high rate performance has been achieved in thin film electrodes;[3-29] but has never been reported in such thick V_2O_5 electrodes. This excellent rate-capability is attributed to efficient electrolyte transport, fast lithium diffusion, and good electronic conductivity developed in the robust CNT/nanowire network.

Towards high-performance flexible devices, it is essential, but challenging, to make thick electrodes (>100 μm) with well-maintained capacity, rate-capability and cycling stability. The interpenetrating ultra-long CNT/nanowire network structure can realize this mission. Herein, CNT/V_2O_5 composite electrodes with 25 wt% CNTs and a thickness of ~130 μm were made and tested in coin-cells. As shown in Fig. 4a, the electrodes show a reversible capacity of ~280 mA h g^{-1} at a low rate of 0.5 C. Similar to thin electrodes, the capacity degrades slowly after 10 cycles at this rate. Nevertheless, after the initial drop, a

reversible capacity of 120 mA h g^{-1} is achieved at 5 C with very slow capacity fading. Even after 200 cycles at 5 C, the electrode still maintains 87% (104 mA h g^{-1}) of its initial capacity at 5 C, suggesting an excellent stability during high-rate cycling. The Coulombic efficiency was only 92% at the first cycle, which is commonly observed for lithium-storage electrodes due to the irreversible replacement of protons and formation of some solid–electrolyte interface.[3-30–32] Nevertheless, the efficiency reached ~100% from the second cycle and was maintained at ~100% during the following cycles, suggesting a high reversibility. Note that, for V_2O_5-based lithium electrodes, a common issue is capacity fading due to the structure and volume changes, which often results in more than 20% of the capacity loss within 100 cycles.[3-14,22–27] These ultra-long-CNT based composites, though, show high mechanical strength and strain tolerance, consequently providing the electrodes with significantly enhanced cycling stability. In contrast, composites made by physically mixing V_2O_5 nanowires with short CNTs have much lower capacity and poor cycling stability.[3-14,15] Based on these studies, it is reasonable to conclude that mechanical robustness is essential for ensuring electrode cycling stability.

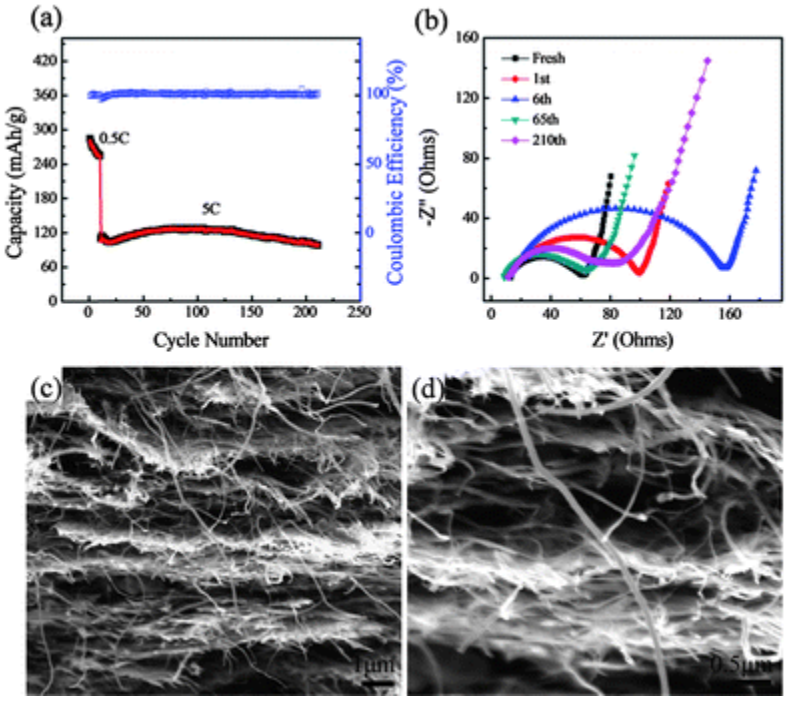

Fig. 3-4 (a) Cycling performance of a CNT/V_2O_5 electrode with 25 wt% CNTs and a thickness of ~130 μm. (b) Nyquist plots of the CNT/V_2O_5 electrode at different cycling stages. (c and d) Cross-sectional SEM images of the CNT/V_2O_5 electrode after 210 cycles.

To further understand the structure and interface stability of our nanocomposite electrodes during cycling, electrochemical impedance spectroscopy (EIS) was conducted along with galvanostatic charge/discharge (Fig. 4b). The Nyquist plots exhibit a single semicircle at high frequency, which is due to a combination of a resistance, capacitance, and constant phase element of the electrode. The ohmic resistance of the electrode is nearly constant during cycling, indicating good contact between the current collector and the electrode, as well as structure integrity of the electrode. The charge transfer resistance (diameter of the semicircle) increases from 50 Ω to 150 Ω after 6 initial cycles due to

solid–electrolyte-interface (SEI) formation and proton replacement during initial cycles.[3-30–32] This causes some irreversibility and capacity fading, agreeing well with the charge/discharge results. Very interestingly, the internal resistance of the electrode decreases to its initial value after 65 cycles, whereafter the charge/discharge capacity increases, which suggests that the CNT/nanowire network structure forms a robust and stable electrode. The decreased electrode resistance after 6 cycles may be due to removal of the protons from the electrodes and a better CNT–V_2O_5 interface induced by the charge/discharge process. In the following cycles, the resistance is relatively stable and accordingly, electrode capacity was well maintained. To further confirm the electrodes' structure integrity, the lithilated electrode (electrode discharged to 1.8 V) and the electrode cycled for 210 cycles were taken out of the coin-cells and examined under SEM. As shown in Fig. S9† and 4c and d, the electrodes retained their initial multilayered structure with an interpenetrating network, further confirming the mechanical robustness.

Conclusions

In summary, we have demonstrated an efficient synthesis of highly robust, flexible, binder-free electrodes based on interpenetrative nanocomposites of V_2O_5 nanowires and ultra-long CNTs. Such robust network architecture enables effective charge transport and electrode integrity, endowing the electrodes with high capacity, high rate-capability and excellent cycling stability for high-performance flexible device applications.

Acknowledgements

This work was partially supported by the China National Program (2011CB932602) and the Center for Molecularly Assembled Material Architectures for Solar Energy

Production, Storage and Carbon Capture, an Energy Frontier Research Center funded by the U.S. Department of Energy, Office of Science, and Office of Basic Energy Sciences under award DE-SC0001342.

Chapter 3 references

1. H. Nishide and K. Oyaizu, Science, 2008, 319, 737
2. V. L. Pushparaj, M. M. Shaijumon, A. Kumar, S. Murugesan, L. Ci, R. Vajtai, R. J. Linhardt, O. Nalamasu and P. M. Ajayan, Proc. Natl. Acad. Sci. U. S. A., 2007, 104, 13574
3. F. Meng and Y. Ding, Adv. Mater., 2011, 23, 4098
4. B. G. Choi, J. Hong, W. H. Hong, P. T. Hammond and H. Park, ACS Nano, 2011, 5, 7025
5. L. Hu, J. W. Choi, Y. Yang, S. Jeong, F. La Mantia, L. Cui and Y. Cui, Proc. Natl. Acad. Sci. U. S. A., 2009, 106, 21490
6. L. Hu, H. Wu, F. La Mantia, Y. Yang and Y. Cui, ACS Nano, 2010, 4, 5843
7. G. A. Snook, P. Kao and A. S. Best, *J. Power Sources*, 2011, **196**, 1
8. L. Nyholm, G. Nyström, A. Mihranyan and M. Strømme, *Adv. Mater.*, 2011, **23**, 3751
9. C. Meng, C. Liu, L. Chen, C. Hu and S. Fan, *Nano Lett.*, 2010, **10**, 4025
10. C. Meng, C. Liu and S. Fan, *Electrochem. Commun.*, 2009, **11**, 186
11. Q. Wu, Y. Xu, Z. Yao, A. Liu and G. Shi, *ACS Nano*, 2010, **4**, 1963
12. H. Gwon, H. S. Kim, K. U. Lee, D. H. Seo, Y. C. Park, Y. S. Lee, B. T. Ahn and K. Kang, *Energy Environ. Sci.*, 2011, **4**, 1277 .

13. P. Chen, G. Shen, S. Sukcharoenchoke and C. Zhou, *Appl. Phys. Lett.*, 2009, **94**, 043113

14. K. H. Seng, J. Liu, Z. P. Guo, Z. X. Chen, D. Jia and H. K. Liu, *Electrochem. Commun.*, 2011, **13**, 383

15. H. Liu and W. Yang, *Energy Environ. Sci.*, 2011, **4**, 4000

16. Q. Zhang, W. Zhou, W. Qian, R. Xiang, J. Huang, D. Wang and F. Wei, *J. Phys. Chem. C*, 2007, **111**, 14638

17. Q. Zhang, D. Wang, J. Huang, W. Zhou, G. Luo, W. Qian and F. Wei, *Carbon*, 2010, **48**, 2855

18. Q. Zhang, G. Xu, J. Huang, W. Zhou, M. Zhao, Y. Wang, W. Qian and F. Wei, *Carbon*, 2009, **47**, 538

1. Z. Chen, Y. Qin, D. Weng, Q. Xiao, Y. Peng, X. Wang, H. Li, F. Wei and Y. Lu, *Adv. Funct. Mater.*, 2009, **19**, 3420

2. G. Xu, Q. Zhang, W. Zhou, J. Huang and F. Wei, *Appl. Phys. A: Mater. Sci. Process.*, 2008, **92**, 531

3. Q. Zhang, M. Zhao, Y. Liu, A. Cao, W. Qian, Y. Lu and F. Wei, *Adv. Mater.*, 2009, **21**, 2876

4. A. Cao, J. Hu, H. Liang and L. Wan, *Angew. Chem., Int. Ed.*, 2005, **44**, 4391

5. Y. Hu, X. Liu, J. Müller, R. Schlögl, J. Maier and D. S. Su, *Angew. Chem., Int. Ed.*, 2009, **48**, 210

6. P. Liu, S. H. Lee, C. E. Tracy, Y. Yan and J. A. Turner, *Adv. Mater.*, 2002, **14**, 27

7. Y. Wang, K. Takahashi, K. H. Lee and G. Z. Cao, *Adv. Funct. Mater.*, 2006, **16**, 1133

8. D. Liu, Y. Liu, A. Pan, K. P. Nagle, G. T. Seidler, Y. Jeong and G. Cao, *J. Phys. Chem. C*, 2011, **115**, 4959

9. L. Mai, L. Xu, C. Han, X. Xu, Y. Luo, S. Zhao and Y. Zhao, *Nano Lett.*, 2010, **10**, 4750

10. B. Guo, X. Wang, P. F. Fulvio, M. Chi, S. M. Mahurin, X.-G. Sun and S. Dai, *Adv. Mater.*, 2011, **23**, 4661

11. Y. Liu, M. Clark, Q. Zhang, D. Yu, D. Liu, J. Liu and G. Cao, *Adv. Energy Mater.*, 2011, **1**, 194

12. W. J. H. Borghols, D. Lützenkirchen-Hecht, U. Haake, W. Chan, U. Lafont, E. M. Kelder, E. R. H. van Eck, A. P. M. Kentgens, F. M. Mulder and M. Wagemaker, *J. Electrochem. Soc.*, 2010, **157**, A582

13. Y. Chang, H. Li, L. Wu and T. Lu, *J. Power Sources*, 1997, **68**, 187

14. G. Ning, B. Haran and B. N. Popov, *J. Power Sources*, 2003, **117**, 160

RECCOMENDATIONS FOR FUTURE WORK

As evidenced by the large volume of projects underway in battery and capacitor materials synthesis, energy materials engineering as a field that doesn't lack recommendations. Suggestions are limited here to a few ideas that immediately relate to the DPSD project:

A. Preparation of DPSD composite materials: to include CNT/microporous carbon composites and sulfur/microporous carbon composites. These composites could be formed in situ or by infiltration. In the case of CNTs, such syntheses would inevitably involve CNT functionalization with "long arm" crosslinkers.

B. Development of Hierarchically Porous carbon based on DPSD: The first steps in this effort have already been taken by templating DPSD with F127 and TEOS. Further development of DPSD as a carbon source en route to hierarchically porous carbon should be explored due to the ease with which it establishes regular microporosity. Co-condensation with TEOS and SiCl4 are both interesting routes because the molecules share Si centers with DPSD. A major hurdle to overcome here is the increasing hydrophobicity of PdPhs as it condenses, rendering it incompatible with many common templates.

C. Activation of the DPSD carbon using common activating agents such as KOH to form spongy carbon with applications as an absorbent.

D. Aerosol processing of DPSD: Spherical microporous carbon is desirable for its packing capabities as well as enhanced surface activity. Aerosol processing of the precursor in the manner reported (i.e. catalyzed condensation) would then

enhance the performance of PdPhs products. Also, should suitable aerosol conditions and ratios be determined, it could be possible to eliminate the hydrophobic/hydrophilic phase separation that occurs in this system during templating and hence carry out recommendation B. In doing so, precursor/ template ratios could be varied, giving rise to a series of hierarchically porous carbons that could be studied to better understand the role of porosity in supercapacitor performance.

APPENDIX

DPSD description

Diphenylsilane diol (DPSD) is a silanol whose crystals are triclinic of the space group pĬ, and has a wide range of uses including as a comonomer with dimethyl siloxanes (Gädda, et. al) to form various synthetic rubbers and as an anticonvulsant drug (Fawcett, et. al). It exists at room temperature in the form of a white powder and has an average melting point off 144˚C, though melting point varies with rate of heating and a flash point of 53˚C (Hyde, et. al(. Its decomposition products include carbon oxides and silicon oxides.

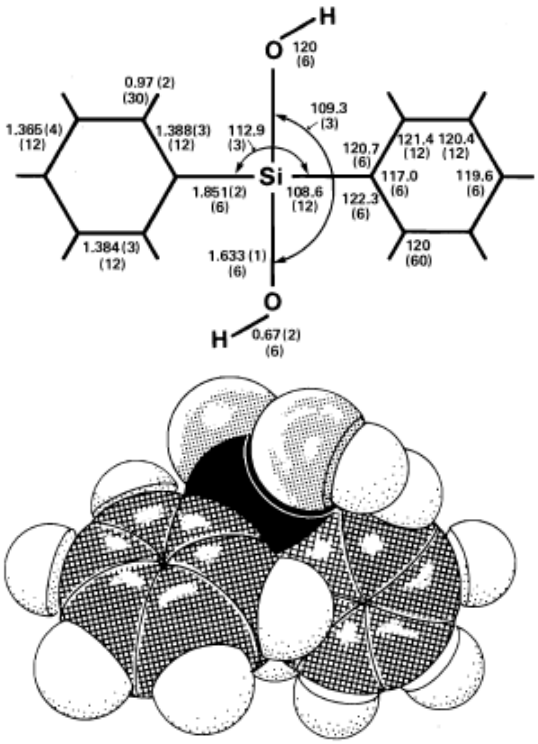

Figure 1: Diphenylsilane diol schematic (left) and space filling model (right) (Fawcett, et. al)

DPSD can self condense into both cyclic and linear products, with the latter tending to be products of low molecular weight. For example, in the presence of small amounts of organostannoxane catalyst, the cyclic tetramer octaphenylcyclotetrasiloxane is primarily formed [4-1]. Organometallic catalytic synthesis of the ring strained hexaphenylcyclotrisiloxane cyclic trimer has also been reported.

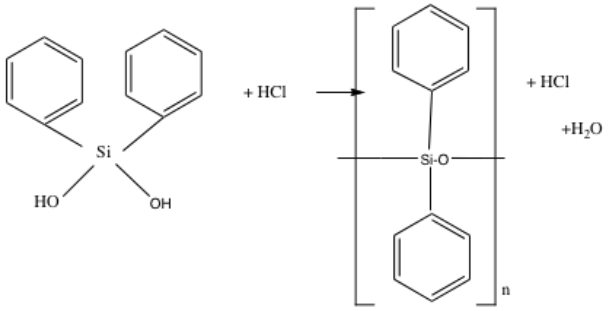

Figure 2: acid catalyzed condensation of DPSD into PdPhs

The linear condensation product of DPSD is poly(diphenylsiloxane) or PDPhs. Anionic ring opening polymerization of its cyclic tetramers is the most successful approach to date for obtaining high molecular weight, linear PDPhs [4-2-4]. To our knowledge, the pyrolysis of condensed DPSD has not been reported.

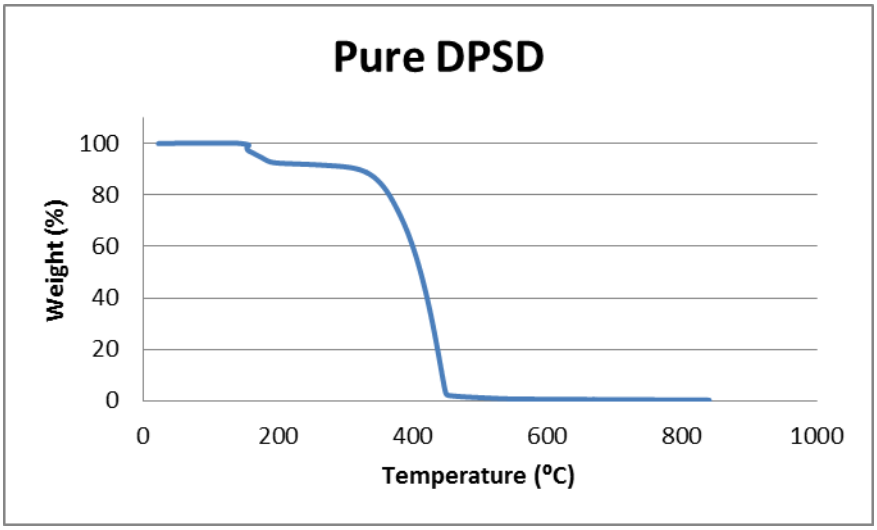

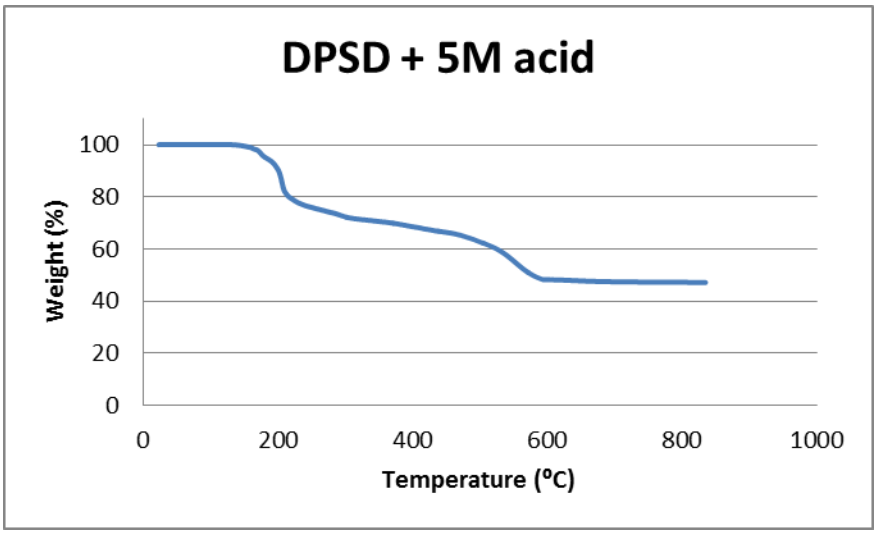

The above TGA thermograms depict the degradation (top) and acid-catalysed condensation (bottom) in an argon atmosphere. The top thermogram has two steps: first, between 180 and 200 degrees, moisture is liberated from this commercially obtained precursor that is stored in ambient conditions. Then, DPSD vaporizes around 400 degrees.

The bottom thermogram shows a similar liberation of water between 180 and 200 degrees, however, the amount of water that is liberated is greater because additional

water is expelled during DPSD condensation. Condensation continues as temperature increases and the precursor that doesn't condense is pyrolyzed up to 600˚ C, at which point the carbonized PdPhs is stable.

General Synthetic Protocol

Condensation of the chosen precursor, DPSD, followed by carbonization and etching of silicon moeities constitutes the microporous carbon syntheses at hand. Syntheses proceed via the following steps:

1. Condense DPSD in solution under acidic or basic conditions in the presence of 5-10 mole parts water per mol DPSD to form elastomer: The condensation of silanols is both acid and base specific. Mild to moderate acid and base catalysts ranging from 0.1 to 2.0 molar in strength can be used. DPSD is highly soluble in polar dioxane and is also mildly soluble in tetrahyrofuran, acetone and ethanol. While dilution doesn't majorly influence condensation, dilution to the upper solubility limit (i.e. 1g DPSD in 2.5 g dioxane or 5 g ethanol) is advisible. DPSD should be fully dissolved in the chosen solvent and the acid or based catalyst that has been diluted in the desired amount of water should be added while the solution is mechanically stirred.

   A typical recipe for acid condensed DPSD would be:

   "1.0g DPSD, 2.5 g dioxane, 0.42 g water, 32 ul concentrated HCL

   And for base condensed DPSD

   "1.0 g DPSD, 2.5 g dioxane, 0.42 g water, 0.07 g KOH pellets

If TEOS is being incorporated into the DPSD, adding 2:1 mol ratio DPSD:TEOS is a good starting point.

2. Let precursor solution stir for our hours covered
3. Pour solution into petri dishes and evaporate solvent (which promotes further condensation) at room temperature overnight.
4. Introduce xerogels (obtained from solvent evaporation) into a standard oven at 120˚C for 24 hours.
5. Put xerogels in a crucible and secure in the center of a vacuum-tight tube furnace. Flush the chamber with nitrogen. Ramp temperature to 900 °C over the course of three hours and then hold for several hours, flushing nitrogen through the chamber throughout the process. Precise carbonization temperature, ramp rate and holding time are all variables of interest that affect the final product morphology. Keep the product under nitrogen while cooling; cool to below 40 C.
6. Etch silica from the product using either a 15% by weight HF infusion at room temperature left overnight, or using a series of sodium hydroxide washes at 60°C. Rinse the resulting material thoroughly in deionized water and dried in a vacuum oven.
7. Grind the resulting microporous carbon into a fine powder using high-energy ball milling. Then, per standardized electrode fabrication protocol, combine it into a slurry of which it constitutes 80 mass percent. Add 10 percent poly(vinylidene fluoride) (PVDF) as the binder and 10 percent carbon black as conductive diluent.

Use N-methyl pyrrolidone (NMP) as the dispersing medium. Apply around 5 mg of the slurry to either nickel foam tape or titanium tape and then placed electrodes in a vacuum oven at 80 Celsius overnight to evaporate the NMP.

Electrochemical Testing Notes:

*See chapter one experimental section for electrode preparation protocol.

*When setting up the cell, be sure that no wires cross, that the working and counter electrode are "in communication" (i.e. close to and facing one another), and that electrodes are fully wetted by electrolyte. Also monitor that electrolyte doesn't rise too far up the electrodes via capillary force.

*Note the open circuit potential of your cell before commencing testing. If it is aberrant, then check the cell and software, making corrections until a reasonable OCP is achieved.

*For cyclic voltammetry, perform two scans at the desired rate and discard the first cycle.

*Start at a low scan rate (i.e. 2 mV/s) and progressively increase the rate in subsequent tests (i.e. 5, 10, 20, 50, 100 mV/s).

*Monitor the first several cycles for any unexpected oxidation peaks, especially at each end of your voltage range, which likely correspond to degradation of electrodes.

*After you've completed CV and any other desired tests (i.e. GPLC), remove working, counter and reference electrodes, rinsing them well in deionized water and drying them to prevent corrosion by the electrolyte. Counter electrode should be stored in a clean, dry container and reference electrode should be stored in a 1M NaCl solution.

*To calculate capacitance from CV curves, integrate the area under the curve, normalizing for weight by dividing the current by the weight of your electrode. Multiply

by 1,000 to convert from mV to V and divide by (scan rate (mV/S)*(2)*(fraction sample)*(voltage window)). The two is for the charging and discharging, fraction sample is the portion of the sample that is active electrode material (usually .8-.85) and the voltage window is obtained by subtracting the lowest potential scanned to from the highest (i.e. a scan from -1.2 to 1.3V has a voltage window of 2.5V).

Appendix references:

1. Beckmann, J.; Jurkschat, K.; Rabe, S.; Shürmann, M.; Dakternieks, D. and Duthie, A. Organometallics 19 (17) 3272-3279 (2000)
2. Gädda, T. and Weber, W. Science and Technology of Silicones and Silicone-Modified Materials ch7, 82-99 (2007)
3. Gädda, T. and Weber, W. Journal of Polymer Science: Part A: Polymer Chemistry 3629-3639 (2006)
4. Harkness, B.; Tachikawa, M.; Yue, H. and Mita, I. Chem. Mater. 10(6), 1700-1705 (1998)
5. Diphenylsilanediol; MSDS no. D213705[online]; Aldrich; Saint Louis, MO, 07/24/2010, sigma-aldrich.com (accessed 03/14/2011)